Nano Research

Open Access

Research Article

Natural biomass-derived conductive e-skin patch for integrated skin-interfacing wearable bioelectronics and smart wound healing

Xugang Dang[1,§,✉], Yufei Fei[1,§], Haijun Wang[1], Xuechuan Wang[1], Meiyuan Tao[2], and Manhui Zheng[2,✉]

[1] *Institute of Biomass and Function Materials & National Demonstration Centre for Experimental Light Chemistry Engineering Education, College of Bioresources Chemistry and Materials Engineering, Shaanxi University of Science and Technology, Xi'an 710021, China*

[2] *School of Pharmaceutical Sciences, Key Laboratory of Biotechnology and Pharmaceutical Engineering, Wenzhou Medical University, Wenzhou 325035, China*

[§] *Xugang Dang and Yufei Fei contributed equally to this work.*

Cite this article: *Nano Research*, **2026**, *19*, 94908706. https://doi.org/10.26599/NR.2026.94908706

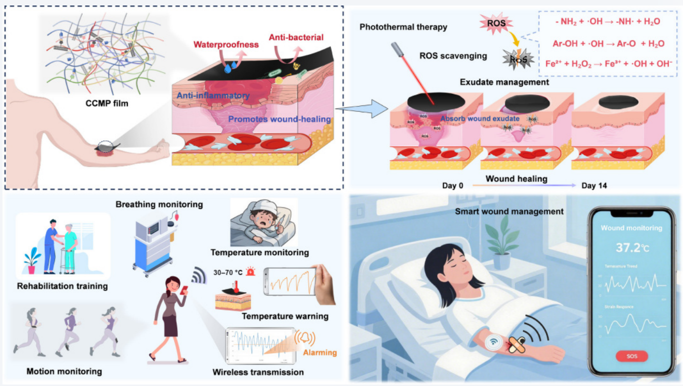

ABSTRACT: As demands for high-quality wound management, health monitoring, and intelligent interaction rise, e-skin—designed to replicate human skin's flexibility, self-healing ability, and multimodal sensing functions—has steadily emerged as a prominent new research focus. Here, we present a natural biomass-derived multimodal conductive e-skin patch (CCMP) that was fabricated by integrating aminated multi-walled carbon nanotubes (MWCNTs-NH_2) and dopamine (DA) into carboxymethyl starch (CMS)/carboxymethyl chitosan (CMCS)/polyvinyl alcohol (PVA) matrix through supramolecular interactions assembly. The CCMP demonstrated remarkable electrical conductivity (24.1 S/m), efficient photothermal conversion (with a heating time constant τ_s = 66.66 s), strong antioxidant activity (> 95.50%), effective antibacterial performance, hydrophobicity, electromagnetic shielding capability, as well as high sensitivity to temperature (temperature coefficient of resistance (TCR) = −8.58%/°C), strain, and electrical signals. Furthermore, the CCMP also demonstrated ultra-high swelling properties. Notably, the CCMP presented easy re-shaping and ultra-high swelling capacity (water sorption reached 1374%), promoting the rapid absorption of tissue exudate. Meanwhile, the CCMP can significantly promote wound healing and reduce pro-inflammatory factor levels, achieving an exceptional 98.21% healing rate within 14 days. We additionally integrate a portable wireless wearable sensing system that can transmit real-time wound status micro-motion and multimodal physiological signals (temperature, stress-strain, respiration, motion, and bioelectric signals) via Bluetooth to computers or mobile devices, thus achieving integrated skin-interfacing wearable bioelectronics and smart wound healing. Overall, this study pioneers a novel approach for wireless wound monitoring system, advancing human-friendly e-skin patch development from single-functional devices to a human–machine–environment intelligent symbiosis system.

KEYWORDS: natural biomass, electronic skin patch, personal thermal management, human health sensing, wound management

1 Introduction

With the advent of the Internet of Things (IoT) and fifth-generation (5G) era, materials science, artificial intelligence, and microelectronics are advancing at a fast pace, fueling human demand for high-quality wound management, intelligent interaction technologies, and bionic robots systems [1, 2]. By emulating the flexibility, self-healing capabilities, and multimodal sensing properties of human skin, electronic skin (e-skin) has gradually emerged as one of the new research directions in the field of flexible electronics [3–6]. Drawing inspiration from human skin, e-skin incorporates stimuli-responsive materials to replicate natural skin's ability to sense, process, and react to external stimuli (e.g.,

Received: December 29, 2025; **Revised:** March 25, 2026
Accepted: April 2, 2026

✉Address correspondence to Xugang Dang, xg.dang@sust.edu.cn; Manhui Zheng, zhengmanh@wmu.edu.cn

pressure, temperature, and humidity) [7, 8]. These capabilities support intelligent functions such as wound management, health monitoring, and human–machine interaction, extensively applied in medical robotics, interactive systems, and continuous physiological surveillance [9].

However, conventional rigid e-skin sensors fabricated from metals and semiconductors fail to meet essential wearing criteria of long-term adhesion, real-time monitoring, wearing comfort, and unobtrusive integration [10]. More critically, they cannot satisfy the growing demand for intelligent functionalities in flexible wearables, such as multimodal sensing, precision health monitoring, and biomimetic interaction [11]. This has, in turn, accelerated the development of next-generation flexible e-skin systems. These systems aim to create intelligent e-skin characterized by shape adaptability, high sensitivity, multifunctional integration, improved performance, and cost-effectiveness. Presently, the field faces a critical imperative: moving beyond single-function devices to develop e-skin with advanced capabilities like multimodal perception, self-healing, and the ability to adapt to changing environments [12].

As a modified starch derivative, carboxymethyl starch (CMS) exhibits significant properties such as unique ionic conductivity (resulting from sodium ion dissociation), excellent mechanical flexibility, superior solution processability, green degradability, and cost-effectiveness [13–15]. Compared with other starch derivatives, CMS is better suited for cutting-edge applications like flexible electronics, wearable devices, and energy storage systems [16]. Owing to its unique properties, it serves as an ideal substrate for flexible electronic films that integrate high performance with sustainability [17]. Aminated multi-walled carbon nanotubes (MWCNTs-NH_2) are chemically modified by introducing amino (–NH_2) groups onto their surfaces to further enhance conductivity [18–20]. MWCNTs-NH_2 also exhibit improved biocompatibility and dispersion. This not only ensures e-skin safety but also sustains the stability and continuity of the conductive network, further enhancing its potential for wider use in the flexible wearable field [21]. Polydopamine (PDA), a biomimetic material inspired by mussel adhesion proteins, features surface-rich phenolic hydroxyl (–OH) and amino (–NH_2) groups [22]. This composition grants it excellent biocompatibility, antibacterial properties, and efficient photothermal conversion capabilities. Carboxymethyl chitosan (CMCS) is synthesized from chitosan via carboxymethylation, which introduces carboxyl (–COOH) groups while preserving amino (–NH_2) groups [23]. Endowed with tunable functional groups, adjustable film-forming performance, excellent electrochemical activity, biocompatibility, and environmental friendliness, CMCS has emerged as an ideal material for electronic film applications [24].

In this study, a multimodal conductive e-skin patch (CCMP) based on CMS was developed by incorporating functional materials—MWCNTs-NH_2, PDA, CMCS, and polyvinyl alcohol (PVA). This system demonstrated excellent photothermal conversion efficiency, notable antibacterial properties, superb swelling resistance, and multimodal sensing capabilities characterized by high sensitivity and signal stability [25]. It could be applied to wound management scenarios such as touch detection, bending motion sensing, temperature warning, and medical monitoring (Fig. 1). As an eco-friendly e-skin patch composed of natural macromolecular materials, the CCMP developed in this study offered five distinct advantages: (1) By aligning with green sustainability principles and utilizing renewable natural biomass resources (such as CMS, CMCS, and dopamine (DA)) as raw materials, both environmental friendliness and biosafety were achieved. (2) Featuring ultra-high swelling capacity, this e-skin patch could quickly absorb wound exudates and simultaneously maintain a balanced moist wound microenvironment, especially advantageous for heavily exuding wounds. (3) By integrating multi-component functional materials (MWCNTs-NH_2/PDA/CMCS/PVA) with bionic structural design, the prepared e-skin patch achieved simultaneous high conductivity and mechanical adaptability, enabling multimodal sensing, personal thermal management, as well as real-time wound-status monitoring and treatment within a single flexible device. (4) By connecting the e-skin patch to a miniaturized electronic chip, a portable wireless wearable system was established. This system can transmit real-time signals (including wound micro-movements and local temperature changes) via Bluetooth to computers, mobile devices, or iPads, forming a complete perception–collection–transmission–terminal system. This innovative approach pioneered human-friendly e-skin technology, opening new avenues for personalized medical electronics in intelligent medicine, such as implantable sensing, diagnosis, and treatment. (5) By incorporating collaborative progress in materials science, artificial intelligence, and microelectronics, this technology enabled the creation of a functional, intelligent flexible wearable device. Overall, the present research aims to advance e-skin development from single-function devices toward a human-machine–environment intelligent symbiosis system, offering novel perspectives on flexible e-skin patches for integrated skin-interfacing wearable bioelectronics and smart wound healing.

2 Experimental

2.1 Chemicals and Materials

Carboxymethyl starch (CMS, CAS: 9063-38-1), carboxymethyl chitosan (CMCS, CAS: 83512-85-0), dopamine hydrochloride (DA, CAS: 62-31-7), polyvinyl alcohol (PVA, CAS: 9002-89-5), 1-(3-dimethylaminopropyl)-3-ethylcarbodiimide (EDC, CAS: 25952-53-8), N-hydroxysuccinimide (NHS, CAS: 6066-82-6), N,N,N',N'-tetramethylethylenediamine (TEMED, CAS: 110-18-9), glycerol (CAS: 56-81-5), and 2,2-diphenyl-1-picrylhydrazyl (DPPH, CAS: 1898-66-4) were purchased from Shanghai Macklin Biochemical Co., Ltd. (Shanghai, China). Aminated multi-walled carbon nanotubes (MWCNTs-NH_2, model: XFM62-1, amino content: 0.4 wt.%–0.6 wt.%) were purchased from Jiangsu Xianfeng Nanomaterials Technology Co., Ltd. (Nanjing, China). Phosphate buffered saline (PBS) (pH 7.2–7.4) was purchased from Shaanxi Zhonghui Hecai Biomedical Technology Co., Ltd. (Shaanxi, China). Simulated body fluid (SBF) (sterile) was purchased from Fuzhou Fhygene Biotechnology Co., Ltd. (Fujian, China). *Escherichia coli* (*E. coli*) and *Staphylococcus aureus* (*S. aureus*) were obtained from the College of Food Science and Engineering, Shaanxi University of Science and Technology. The mice and rats used in animal experiments are clean-grade C57BL/6 male mice provided by Beijing Vitone Lihua Laboratory Animal Technology Co., Ltd. (Beijing, China).

2.2 Preparation of multimodal conductive e-skin patch (CCMP)

As shown in Fig. 1(a), 2 g of CMS was mixed with 30 mL of

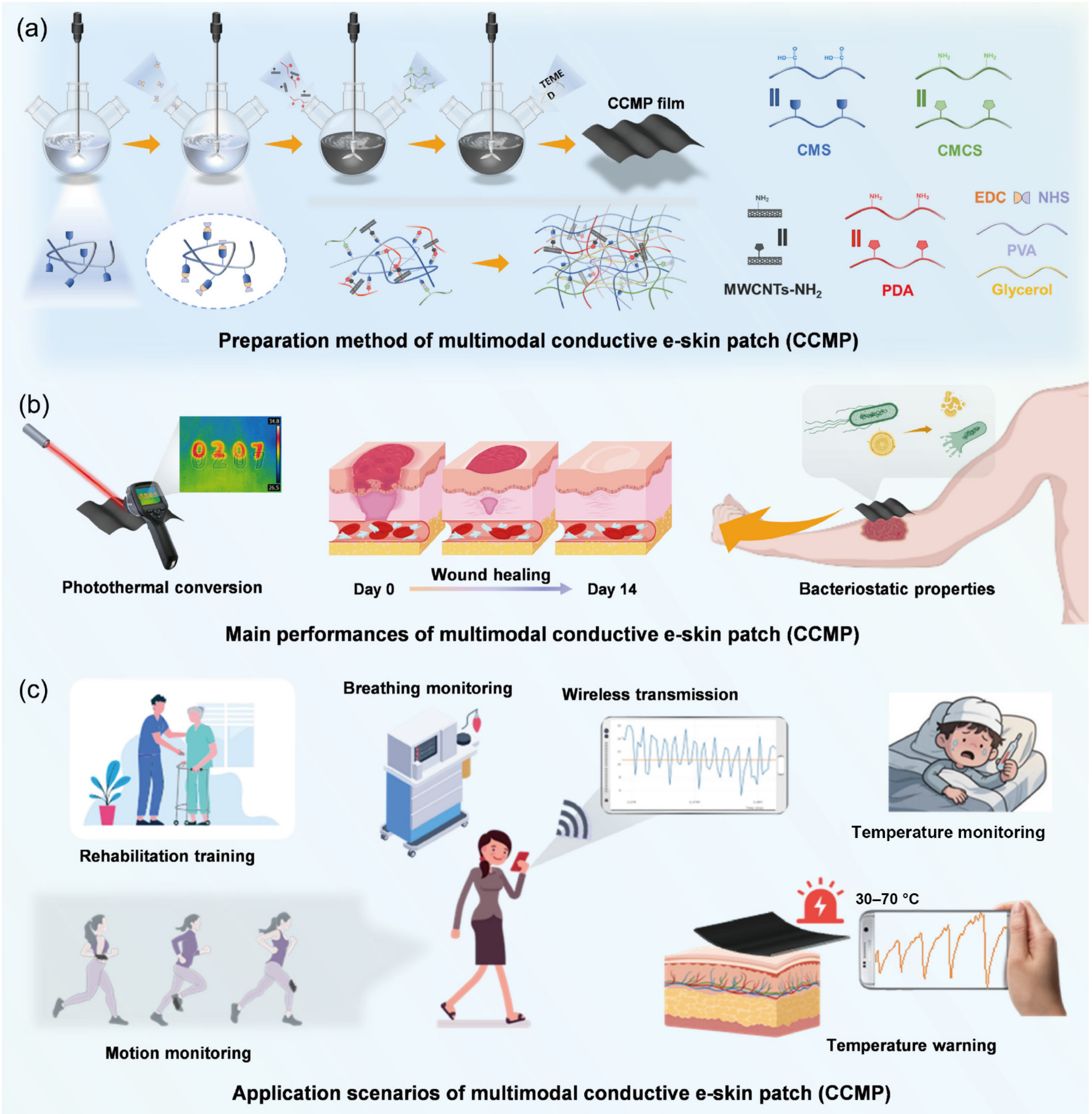

Figure 1 (a) Preparation method, (b) main performances, and (c) application scenario of CCMP.

deionized water. The mixture was stirred continuously and gradually heated to 70–80 °C, followed by stirring for approximately 0.5 h to obtain a CMS dispersion. Subsequently, EDC and NHS (a molar ratio of 1:1) were dissolved separately in 3 mL of deionized water to obtain EDC and NHS solutions. The EDC and NHS solutions were then poured into the CMS dispersion and stirred at room temperature for 0.5 h to activate the carboxyl groups of CMS molecules. Next, MWCNTs-NH_2 and DA were dispersed in deionized water to obtain a homogeneous suspension. This mixed suspension was then slowly poured into the activated CMS dispersion and stirred for 1 h. The carboxyl groups of CMS underwent amidation with the amino groups of both MWCNTs-NH_2 and DA via the EDC/NHS coupling reaction, achieving molecular cross-linking and stable fixation. Then, CMCS and PVA were stirred at a high temperature of 85–95 °C until completely dissolved to yield the CMCS and PVA solutions. Afterward, the CMCS and PVA solution was successively added to the main mixture, followed by adding 10 drops of TEMED to catalyze the polymerization of DA monomers. Subsequently glycerol was incorporated, and the mixture was stirred continuously for another hour to promote uniform homogeneous system, resulting in the preparation of a natural biomass-derived conductive composite precursor.

Finally, the prepared natural biomass-derived conductive composite solution was poured onto a polytetrafluoroethylene plate (10 cm × 10 cm) and dried naturally at room temperature for 72 h to obtain a natural biomass-derived CCMP. The resulting e-skin patch materials were designated as CCMP-0, CCMP-1, CCMP-2, CCMP-3, and CCMP-4, their respective raw material compositions and dosages are provided in Table S1 in the Electronic Supplementary Material (ESM). CCMP-0 served as the control group in subsequent characterization tests.

2.3 Characterization of CCMP

The Fourier transform infrared spectroscopy (FT-IR), X-ray diffraction (XRD), X-ray photoelectron spectroscopy (XPS), thermogravimetric analysis, and surface morphology were tested to study the structure feature of the multimodal conductive e-skin patch (CCMP). The characterization methods in detail were shown in the supporting information.

2.4 Application performance of CCMP

Mechanical properties, tailorability, antioxidant activity, conductivity properties, water contact angle, swelling behavior (water contact angle, water absorption rate, swelling property, and wound exudate absorption rate), light transmittance, antibacterial properties, biocompatibility, hemolytic, wound healing properties, anti-inflammatory effect, electromagnetic shielding performance (the frequency range of 8.2–12.4 GHz), photothermal conversion performance (the near-infrared (NIR) laser with a wavelength of 980 nm), and sensing performance (using a two electrode test cell to study the effects of human physiological signals) of the multimodal conductive e-skin patch (CCMP) were investigated to uncover its sustainable utilization in integrated wearable smart patches and skin bioelectronics. The testing methods in detail were shown in the supporting information. Informed consent was obtained from the volunteer participants involved in this experiment. Volunteers signed consent to participate in sensor test experiments.

2.5 Statistical analysis

The research used ANOVA methods combined with Tukey's test to compare more than two data sets. All experiments were performed in triplicate and results are reported as mean ± standard deviation. In addition, synthesis and tests were run in triplicate, and the average values were taken.

3 Results and discussion

3.1 Design and characterization of CCMP e-skin patch

Figure 2(a) and Fig. S1 in the ESM present the infrared spectra of CCMP and raw materials, respectively. The peak at 3312 cm^{-1} was attributed to the O–H stretching vibration in the polysaccharide backbone [26, 27]. The characteristic peak at 2900 cm^{-1} corresponded to the asymmetric and symmetric stretching vibrations of C–H. Within the system, CMS and CMCS contained abundant carboxyl groups. Consequently, aside from the very broad O–H peak related to carbonyl stretching vibration, the characteristic peaks at 1706 and 1589 cm^{-1} (assigned to C=O) and those at 1104 and 1033 cm^{-1} (corresponding to C–O stretching vibration) intensified with increasing CMCS content [24]. Additionally, the double peaks at 1282 and 1462 cm^{-1} were attributed to the symmetric and asymmetric stretching vibrations of –COOH in CMS and CMCS [6]. In contrast to the raw materials, CCMP samples exhibited new absorption peaks at 1589 cm^{-1} (amide II band) and 1282 cm^{-1} (amide III band), likely due to amidation reactions between amino groups in PDA and MWCNTs-NH_2 and carboxyl groups in CMS and CMCS molecules, which formed amide bonds. Accordingly, as the content of introduced amino groups increases, the characteristic quinone (C=O) peak at 1589 cm^{-1} decreases, while the C–N bond peak at 1250 cm^{-1} increases. Moreover, the C=O characteristic absorption peak in the CCMP sample exhibits a redshift. Specifically, the C=O peak originally at 1608 cm^{-1} in CMS shifts to 1589 cm^{-1} [28]. This shift is due to intramolecular hydrogen bonding between the phenolic hydroxyl groups in PDA and the –COOH groups in CMS and CMCS [29]. The hydrogen bonding reduces the electron density of the C=O bond and weakens its strength, resulting in the observed redshift.

The XRD patterns of CCMP and raw materials are presented in Fig. 2(b) and Fig. S2 in the ESM. As seen in Fig. S2 in the ESM, CMS exhibits distinct diffraction peaks at 2θ values of 15°, 17.4°, 20°, 22.8°, 31.5°, and 45.2° [30]. The broad peaks at 17.4° and 22.8° are associated with amorphous regions formed by the disruption of crystalline order during starch etherification. In Fig. 2(b), the CCMP samples show diffraction peaks at 20.7° and 25.9°. The intensity of the peak at 20.7° gradually increases with higher CMCS and DA content [31]. Compared to CMS, the CCMP sample exhibits a broader and partially diminished diffraction envelope at 20.7°, suggesting that functional groups may have influenced crystal cross-linking. This restriction in molecular chain mobility reduced structural order and weakened crystallization. Additionally, the diffraction peak at 25.9° grows more intense with increasing MWCNTs-NH_2 content. This indicates effective intermolecular interactions among CMS, CMCS, DA, and MWCNTs-NH_2, leading to the emergence of diffraction features characteristic of PDA and MWCNTs-NH_2 in the CCMP samples. Notably, in the CCMP-0 sample, which contains no MWCNTs-NH_2 or DA, the peak at 25.9° is absent.

The thermogravimetric (TGA) and derivative thermogravimetric (DTG) curves of CCMP and raw materials are presented in Figs. 2(c) and 2(d), and Fig. S3 and Table S2 in the ESM. The CCMP samples exhibited high thermal stability. As shown in Figs. 2(c) and 2(d), each CCMP sample displayed three major decomposition stages. By comparison with the raw materials (Fig. S3 in the ESM), the first stage was attributed to the evaporation of water. The second stage corresponds to the decomposition of glycerol, CMS, CMCS, and a small amount of MWCNTs-NH_2 [32]. The third stage is associated with the thermal decomposition of DA and PVA. Furthermore, no significant change was observed in the degradation temperature across the CCMP samples. As the content of CMCS, DA, and MWCNTs-NH_2 increased, the weight loss of CCMP within the temperature range of 40 to 600 °C decreased, indicating enhanced thermal stability.

As shown in Figs. 2(e) and 2(f), and Fig. S4 in the ESM, XPS was employed to analyze the chemical composition, bonding environment, binding energy, and elemental distribution of CCMP-0 and CCMP-2, focusing on the C, N, and O elements [33]. The corresponding binding energies and spectral assignments are summarized in Table S3 in the ESM. The full survey spectra of CCMP-0 and CCMP-2 are presented in Figs. 2(e) and 2(f), respectively. Chemical composition analysis reveals that after the incorporation of DA and MWCNTs-NH_2, the content of nitrogen increased significantly, while the levels of carbon and oxygen remained relatively unchanged. Moreover, the peaks corresponding to O 1s, N 1s, and C 1s all shifted toward lower binding energies. This shift suggests enhanced electron density around these atoms, likely due to synergistic effects involving interfacial covalent bonding (e.g., Schiff base formation) and non-covalent interactions. As shown in Figs. S4(a) and S4(d) in the ESM, the content of C–O/C–N groups increased markedly, while that of C=O groups decreased considerably [34]. From Figs. S4(b) and S4(e) in the ESM, a notable increase in the proportions of N–C and N=C groups can be observed, accompanied by a significant reduction in N–H groups. Furthermore, Figs. S4(c) and S4(f) in the ESM clearly indicate the disappearance of the O=C–O peak and an increase in the signals from C–O, C–O–C, C=O, and O–C–O functional

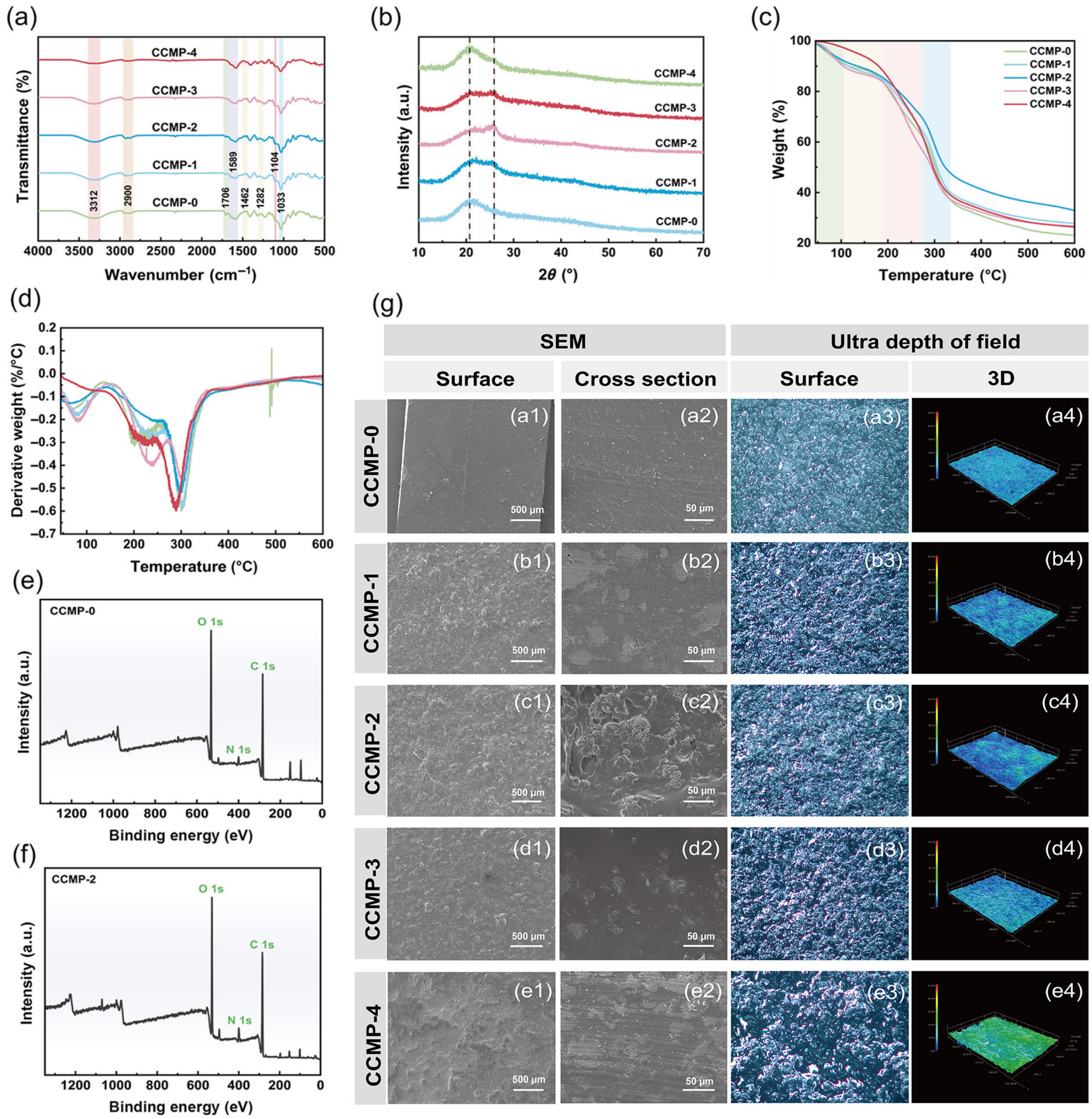

Figure 2 Basic characterization of CCMP. (a) Infrared spectrogram; (b) XRD pattern; (c) TGA diagram; (d) DTGA diagram; (e) XPS full spectrum of CCMP-0; (f) XPS full spectrum of CCMP-2; (g) SEM images and ultra depth of field diagrams of CCMP.

groups [35]. These changes are attributed to the formation of new amide bonds within the system, which reduce the number of C=O groups and enhance the signals related to C–O and N=C moieties in CCMP-2. These XPS findings are consistent with the FTIR results, further confirming the successful synthesis of the multimodal conductive e-skin patch material CCMP.

3.2 Microscopic morphology analysis

As shown in Fig. 2(g), the microstructure, surface flatness, and thickness of the CCMP samples were characterized using scanning electron microscope (SEM) and ultra-depth-of-field microscope. As depicted in Figs. 2(g)(a1)–2(g)(e1), the surface of CCMP-0 appears smooth and flat [36]. With increasing MWCNTs-NH_2 content, the surface becomes noticeably rougher. This increased roughness is attributed to the tendency of MWCNTs-NH_2 to agglomerate within the matrix at higher concentrations, forming micro-scale protrusions. The addition of DA further promotes the dispersion of MWCNTs-NH_2, leading to a smoother surface. This effect is likely due to the polymerization of DA into PDA, which coats the MWCNTs-NH_2 via hydrogen bonding and π–π interactions, thereby reducing agglomeration and promoting a more uniform surface morphology. Notably, micron-sized white particles are observed in the cross-sections of CCMP-0 and CCMP-4. Their presence may be explained by the saturation of hydrogen bonding or electrostatic interactions between CMS and CMCS at higher CMCS concentrations, resulting in incomplete dispersion and self-aggregation of CMCS into micron-scale particles [37]. Alternatively, CMCS itself may exhibit a crystallization tendency. At high concentrations, physical interlinking or microgel structures can form, and these may undergo crystallization or pre-deposition during drying or film formation, ultimately leading to the formation of a white insoluble phase with visible pores in the cross-section. Furthermore, 3D ultra-depth-of-field microscopy was used to examine the surface topography (Figs. 2(g)(a3)–2(g)(e3)). The results are consistent with SEM observations and provide a more intuitive understanding of how variations in MWCNTs-NH_2, DA, and CMCS content influence the microstructure of the CCMP system. As illustrated in Figs. 2(g)(a4)–2(g)(e4), all samples exhibit relatively uniform and flat surface topographies. In particular, CCMP-0 demonstrates high flatness and low roughness, indicating good compatibility between CMS and CMCS at low concentrations.

3.3 Mechanical properties, light transmittance, tailorability, conductivity

As an artificial system designed to mimic the sensory function of human skin, electronic skin must exhibit practical utility and motion adaptability in real-world applications. Accordingly, this study investigated the fundamental properties of CCMP, including its swelling behavior under various conditions. Figures 3(a) and 3(b) present the tensile stress–strain curves of the prepared CCMP. It could be observed that the tensile stress of CCMP initially increased and then decreased, with CCMP-4 achieving a maximum fracture stress of 3.9 MPa. Increasing the CMCS content significantly enhanced the stress performance of the system, attributable to the multi-functional groups of CMCS that formed hydrogen bonds, ionic bonds, or electrostatic interactions within the dynamic physical cross-linking network. However, higher CMCS content also led to a notable reduction in strain, as physical cross-linking restricted molecular chain mobility while improving mechanical strength. Furthermore, CCMP demonstrated considerable deformation capability and excellent stretchability (> 90%), exceeding that of human skin (60%–75%) [38]. Excessive incorporation of DA results in an overly high cross-linking density, which impedes segmental movement and leads to diminished mechanical properties in CCMP-3. Although the addition of conductive fillers partially compromises mechanical strength, a moderate increase in filler content allows the multi-modal conductive e-skin patch to maintain satisfactory stress and strain performance (> 1.5 kPa, > 100%). The resulting CCMP exhibits outstanding flexibility and mechanical softness, enabling conformal contact on curved body surfaces and adaptation to skin dynamics for seamless adhesion.

UV shielding plays a critical protective role in electronic skin, contributing not only to extended device lifespan but also to biological safety, signal stability, and environmental adaptability. As shown in Fig. 3(c), the UV transmittance curve of CCMP demonstrates that the incorporation of MWCNTs-NH_2 and DA enables nearly complete absorption of both ultraviolet A (UVA) and UVB radiation. This capability stems from the π–π conjugated structure in MWCNTs-NH_2, which provides a high-energy UV absorption framework capable of effectively capturing UV photons and converting them into thermal energy. Meanwhile, PDA has a catecholquinone structure similar to natural melanin, which can achieve non-selective absorption of ultraviolet rays in the full wavelength range. The synergistic effect of these two components results in near-zero transmittance (200–800 nm) in the multimodal conductive e-skin patch, achieving comprehensive UV shielding. In contrast, CCMP-0, which contains no fillers, remains highly transparent, showing almost no visible effect when covering printed patterns. Since UV radiation can cause DNA damage, photoaging, inflammation, and even skin cancer, the highly efficient UV shielding property of this CCMP serves as a physical barrier. It helps prevent photo-oxidative damage to newly formed tissues, reduces inflammatory responses, and minimizes secondary injury induced by ultraviolet exposure [39].

The optical image of the tailored CCMP is shown in Fig. 3(d). The material demonstrates excellent shape adaptability, enabling it to be cut into various forms such as carrots, stars, and even intricate

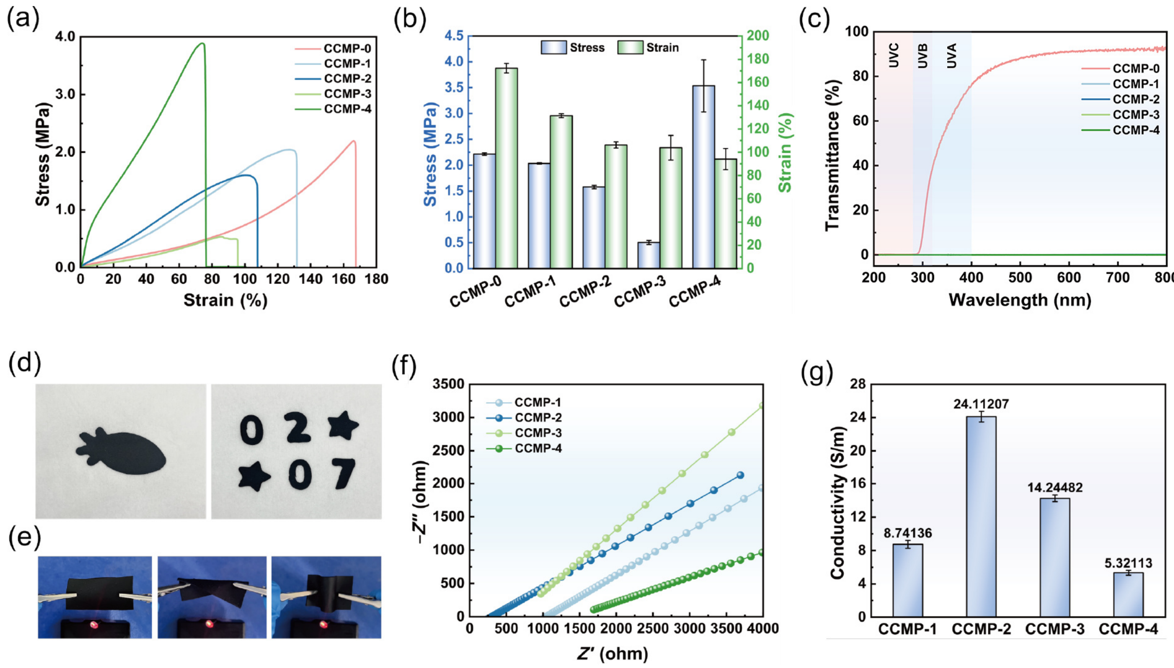

Figure 3 Basic performance of CCMP. (a) The stress–strain curves of CCMP. (b) Mechanical properties of CCMP. (c) The transmittance of CCMP. (d) Optical images of CCMP. (e) Using CCMP-2 as the conductor, the brightness change of the LED is affected by bending 180° and torsion 180°. (f) The fitted CCMP EIS impedance diagram. (g) Conductivity of CCMP.

digital patterns [28]. After cutting, the versatility and multimodal sensing capabilities of CCMP are well preserved, with clean and well-defined edges. This offers a new strategy for developing miniaturized, portable, and customized flexible e-skin patches.

Conductivity is essential for intelligent electronic skin to enable signal transmission, energy supply, and interactive functions. The carboxyl groups (–COO^-) in CMS molecules can ionize in solution to form ionic conduction pathways, yet their solid-state conductivity remains limited. Thus, introducing conductive fillers to form a composite structure is necessary to establish dual electron–ion conduction channels, thereby enhancing overall conductivity. Multi-walled carbon nanotubes subjected to amination treatment exhibit improved electrical conductivity, high chemical stability, and strong antioxidant properties [40]. As shown in Fig. 3(e) and Video S1 in the ESM, when CCMP-2 is used as a conductor, the brightness of the light-emitting diode (LED) remains nearly unchanged under 180° bending and 180° twisting, indicating stable conductive performance under dynamic deformation. This demonstrates the potential of this multi-modal conductive e-skin patch for application in diverse scenarios. To further investigate the influence of MWCNTs-NH_2 content on the conductivity of CCMP, electrochemical impedance spectroscopy (EIS) tests were conducted, as shown in Figs. 3(f) and 3(g). All CCMP samples exhibit high conductivity (> 5 S/m), with CCMP-2 reaching a value of up to 24.1 S/m. The results indicate that the conductivity of CCMP increases with higher MWCNTs-NH_2 content. Moreover, the addition of DA improves the dispersion of MWCNTs-NH_2 within the system and enhances the continuity of the conductive network. This is attributed to the hydrogen bonds formed between the polar functional groups of DA and MWCNTs-NH_2, which inhibit the agglomeration of carbon nanotubes and promote their uniform distribution.

3.4 Swelling behavior (water contact angle, water absorption rate, swelling property, wound exudate absorption rate, water retention performance) and electromagnetic shielding performance

To evaluate the swelling behavior of CCMP, several relevant parameters were experimentally tested, including water contact angle, water solubility, swelling ratio, and wound exudate absorption rate [41]. Figure 4(a) shows the water contact angle

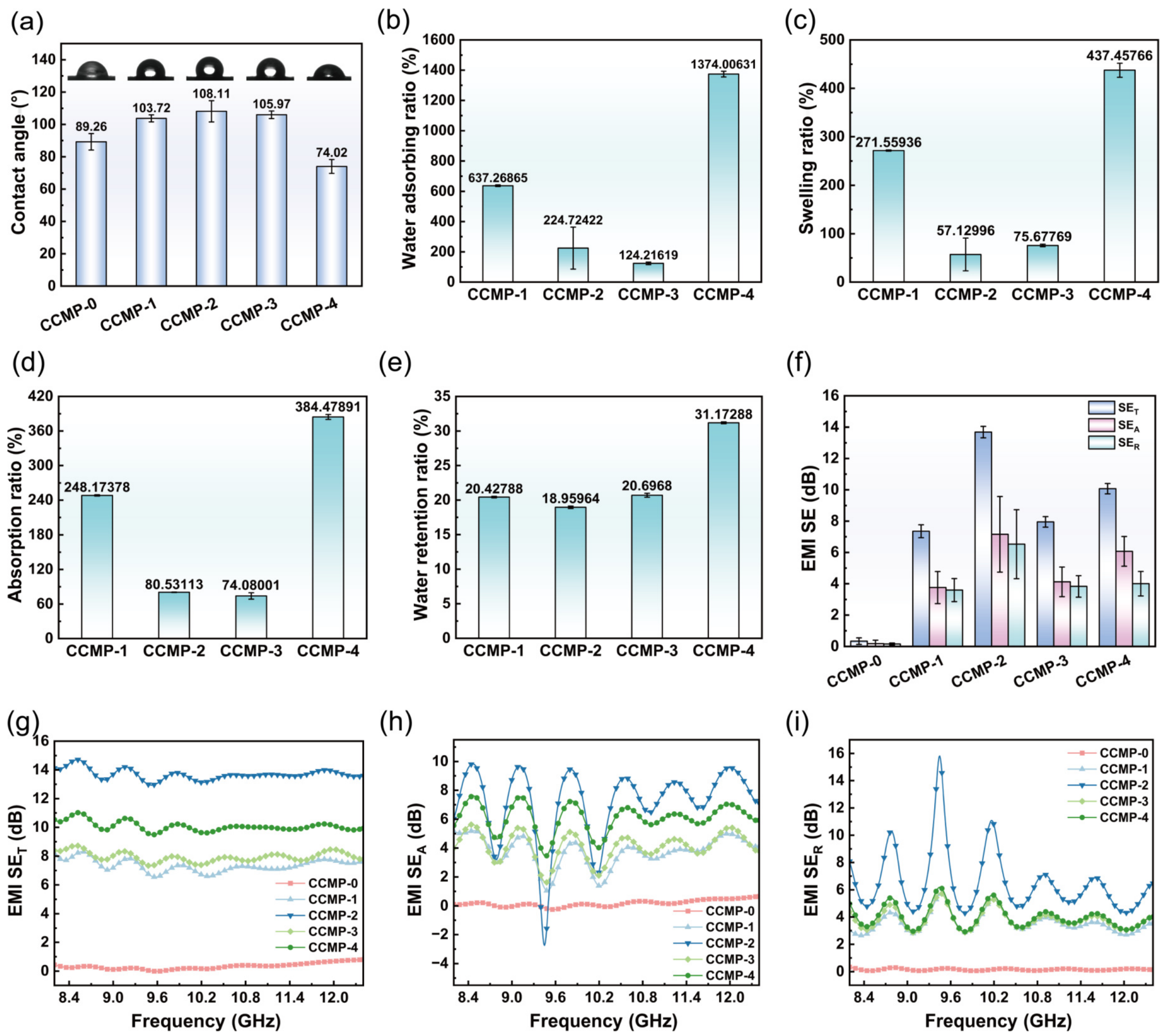

Figure 4 Swelling behavior and electromagnetic shielding performance of CCMP. (a) Water contact angle and optical images of CCMP. (b) The water absorption of CCMP. (c) Swelling ratio of CCMP. (d) CCMP wound exudate absorption rate. (e) The water retention performance of CCMP. (f) The electromagnetic shielding effect of CCMP at 8.2–12.4 GHz frequency. (g) The total shielding effectiveness (SE_T) curve of CCMP at 8.2–12.4 GHz frequency. (h) The absorption shielding effectiveness (SE_A) curve. (i) The reflection shielding effectiveness (SE_R) curve.

(WCA) of CCMP along with corresponding optical images. As the outermost layer of the skin patch material, the surface hydrophobicity of CCMP plays a critical role. The results indicate that the hydrophobicity of CCMP increases with higher MWCNTs-NH_2 content, which modifies the originally hydrophilic nature of CMS and CMCS, making it more suitable for electronic skin applications. Notably, CCMP-2 achieves a water contact angle of up to 108.11°. The wound exudate absorption rate is a key performance metric for medical electronic skin used in intelligent wound management, as it helps maintain a moist microenvironment, facilitates healing, and aids in inflammation control [42]. As shown in Figs. 4(b)–4(e) and Fig. S5 in the ESM, CCMP was immersed in deionized water, PBS, and SBF to simulate sweaty and wound exudate conditions, thereby evaluating its water absorption, swelling behavior, and biological safety. The data clearly show that swelling equilibrium is reached within approximately 1 h. With increasing CMCS content, the water absorption rate in water, swelling ratio in PBS, and absorption in SBF all increase. This enhancement is attributed to the abundance of hydrophilic groups in CMCS, which improve the material's capacity to adsorb water molecules, thereby significantly boosting absorbency and swelling [43]. Conversely, these properties decrease markedly as the content of MWCNTs-NH_2 rises, likely due to agglomeration effects that increase cross-linking density, hindering water penetration and diffusion, and resulting in reduced absorption and swelling. CCMP with high water absorption capacity can effectively absorb wound exudate and adhere to the wound bed, maintaining a moist environment that supports healing [44]. In this study, CCMP-4, with the highest CMCS content, exhibited the most favorable hydrophilic properties (WS = 1374%, SR = 437%, SBF absorption = 384%, WR = 31%). However, excessive CMCS content may compromise mechanical strength. Based on these findings, the tailored swelling behavior of CCMP can effectively mitigate interference from human sweat during physical activity, thereby enhancing operational reliability, signal accuracy, wearing comfort, and service life in real-world sweaty conditions. The low water retention rate of CCMP is due to its rigid hydrophilic network formed by chemical cross-linking, which tends to quickly absorb and temporarily retain water through physical adsorption and capillary, allowing a large amount of free water to escape through evaporation rather than locking it strongly and permanently inside the molecular structure. In this study, the high absorption, high moisture permeability, and low water retention characteristics of CCMP together constitute an active liquid transport system dominated by evaporation. The system can quickly absorb a large amount of exudate and efficiently export water in the form of steam immediately, so as to maintain a dynamic and balanced wet state at the wound interface, effectively solving the risk of impregnation caused by liquid locking of traditional superabsorbent dressings. Furthermore, these properties support its application in intelligent healthcare by maintaining a moist healing environment, absorbing exudate or pus, mitigating inflammatory responses, and helping prevent wound infections.

With electromagnetic shielding capability, the e-skin maintained an "electromagnetically clean" microenvironment that promoted wound healing. This key technical feature blocked external electromagnetic interference, enabling more accurate and stable monitoring, treatment, and wound management [45]. It thereby enhanced treatment safety and patient comfort, while paving the way for future intelligent medical applications. As shown in Figs. 4(f)–4(i), CCMP exhibited notable electromagnetic shielding performance attributed to the incorporation of MWCNTs-NH_2, reaching a maximum of approximately 14.5 dB.

3.5 Photothermal conversion performance

The e-skin showed photothermal conversion capacity, capable of converting light energy—most notably near-infrared radiation—into heat. Beyond enabling thermal regulation, this function also promoted multimodal intelligent responses like wound healing and antibacterial activity [2]. Both PDA and aminated MWCNTs-NH_2 demonstrated excellent photothermal performance and acted synergistically to form an efficient photothermal conversion system [46]. As shown in Fig. 5(a), infrared thermal imaging was utilized to visualize the temperature distribution and variation of CCMP-3 under 980 nm near-infrared light irradiation. Starting from an initial temperature of 22.2 °C in a 25 °C ambient environment, the surface temperature of CCMP-3 rose to 74.3 °C after 60 s of exposure at a laser power density of 1.0 W/cm^2. Figure 5(b) presents temperature–time profiles of different CCMP samples under 980 nm irradiation, illustrating the influence of PDA and MWCNTs-NH_2 on photothermal conversion efficiency. The surface temperatures rapidly reached saturation values of 59.2, 65.6, 79.3, and 62.7 °C, respectively, from an initial temperature of 22 °C. These results indicate that both PDA and MWCNTs-NH_2 enhance the photothermal performance of CCMP, with PDA contributing more significantly. To further investigate the photothermal behavior of CCMP-3, it was irradiated under 980 nm light at various power densities. As depicted in Fig. 5(c), under power densities of 0.6, 0.8, 1.0, 1.2, and 1.4 W/cm^2, the surface temperature of CCMP-3 quickly reached saturation values of 35.1, 51.8, 74.5, 118.2, and 160.2 °C, respectively. This demonstrates that higher laser power densities lead to more rapid temperature increases. Additionally, the temperature change ($T_{max} - T_{surr}$) under different power densities was linearly fitted, revealing a strong positive correlation ($R^2 = 0.977$), as shown in Fig. 5(d).

To evaluate the cycling stability of the photothermal conversion performance, CCMP-3 was subjected to six on/off cycles of 980 nm near-infrared irradiation at a power density of 1.0 W/cm^2, as shown in Fig. 5(e). In each cycle, the maximum temperature reached 75 °C or higher, demonstrating consistent response sensitivity and stable photothermal conversion efficiency, which supports its suitability for long-term wear. As observed in Fig. 5(f), CCMP-3 rapidly heated from room temperature to approximately 66 °C within 15 s. The temperature rise began to stabilize after 50 s, reaching a saturation value of 82.1 °C at 150 s. Upon removal of the infrared source, the surface temperature dropped to 35 °C within 30 s. Based on these data, a linear relationship was plotted between the cooling time and the negative natural logarithm of the driving force temperature (Fig. 5(g)), which showed a strong positive correlation. The system time constant was calculated to be 66.66 s. Figure 5(h) illustrates the photothermal conversion mechanism of CCMP under sunlight irradiation. When exposed to sunlight, PDA and MWCNTs-NH_2 within CCMP act synergistically to convert light energy into heat, leading to a rise in surface temperature that was captured by an infrared thermal camera. Figure 5(i) displays infrared thermal images of CCMP-3 samples cut into different shapes after 10 and 60 s of sunlight exposure at an ambient temperature of 25 °C. The images clearly demonstrate the efficient conversion of light into heat under illumination. In summary, this electronic skin exhibits excellent photothermal conversion performance and cycling stability, paving the way for a new

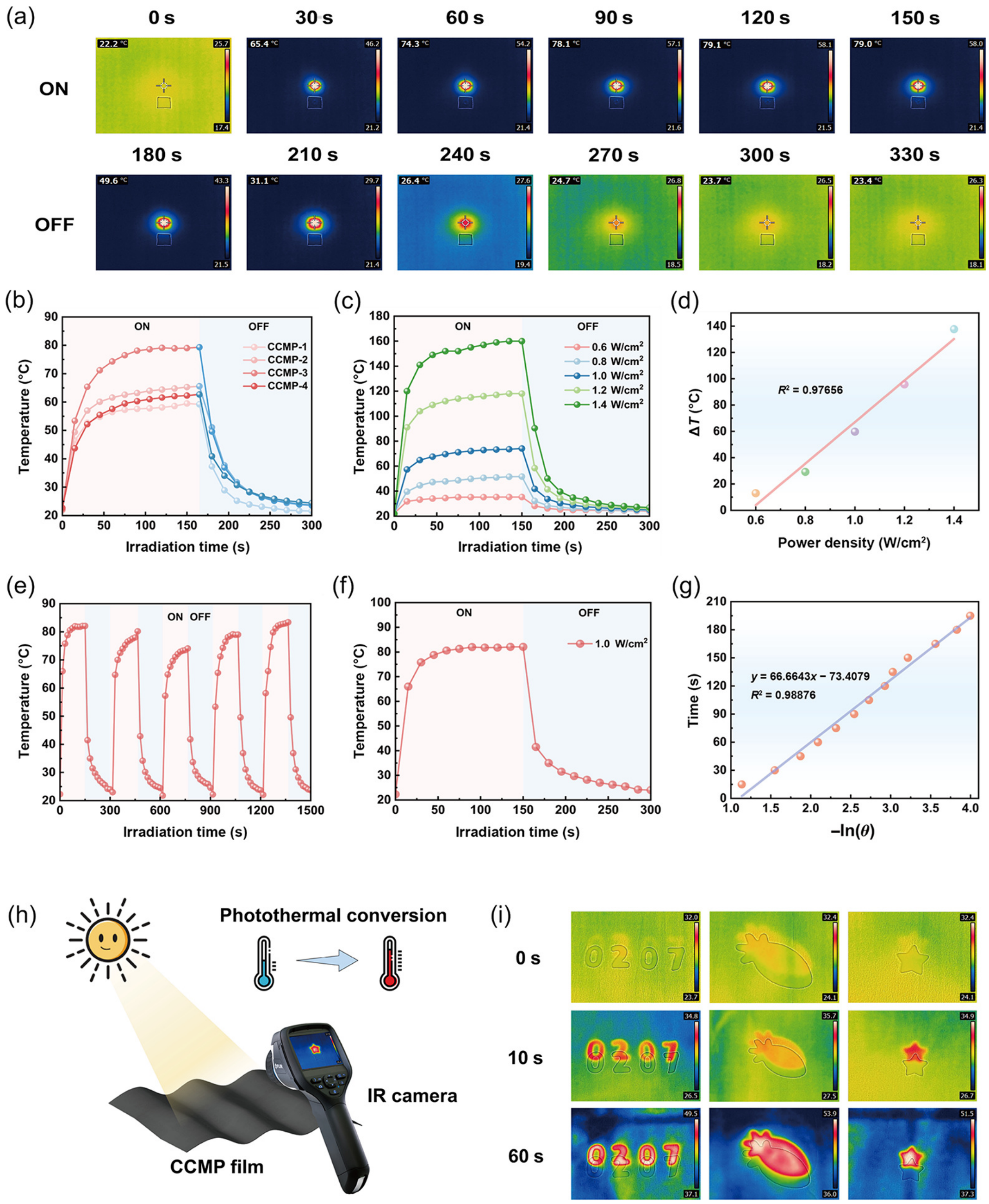

Figure 5 Photothermal conversion performance of CCMP. (a) Infrared thermography of photothermal conversion process of CCMP-3 under 980 nm near-infrared light irradiation (power density: 1.0 W/cm²). (b) The temperature–radiation time curves of different CCMP under 980 nm near-infrared light irradiation. (c) The temperature–radiation time curve of CCMP-3 under 980 nm near-infrared light irradiation with different power densities. (d) Under the irradiation of 980 nm near-infrared light with different power densities, the photothermal conversion temperature of CCMP-3 was linearly fitted with the laser power density. (e) The radiation on/off diagram of CCMP-3 under 980 nm near-infrared light irradiation for 6 cycles (power density: 1.0 W/cm²). (f) Single radiation on/off diagram of CCMP-3 under 980 nm near-infrared light irradiation (power density: 1.0 W/cm²). (g) The relationship between the linear time data of CCMP-3 during cooling under 980 nm near-infrared light irradiation and the negative natural logarithm of driving force temperature (power density: 1.0 W/cm²). (h) Photothermal conversion principle of CCMP under solar illumination. (i) Infrared thermal images of CCMP-3 after cutting at 10 and 60 s of solar irradiation (ambient temperature: 25 °C).

generation of intelligent thermal management systems that are efficient, integrated, and smart.

3.6 Biosafety (*in vitro* antibacterial activity, cytotoxicity, antioxidant activity, and hemolytic activity)

The outstanding biosafety of flexible e-skin patches is essential for their long-term non-invasive application on human skin and supports their broad adoption in intelligent medical care and wound management [47]. To assess the biosafety of CCMP, the material's *in vitro* antibacterial activity, biocompatibility, antioxidant capacity, and hemolytic properties were hereby evaluated. As shown in Fig. 6(a), the antibacterial performance of CCMP samples was tested against Gram-negative *Escherichia coli* (*E. coli*) and Gram-positive *Staphylococcus aureus* (*S. aureus*). No inhibition zones were observed in the blank control group or CCMP-0, indicating a lack of inherent antibacterial activity. However, a noticeable reduction in bacterial count was detected under CCMP-0, likely due to the presence of CMCS. In contrast, all CCMP samples containing PDA displayed clear inhibition zones. While some zones showed blurred edges (a result of the material's high water absorption), visual inspection of the optical images indicated the strongest antibacterial effect of CCMP-3. The diameters of the inhibition zones were measured and statistically analyzed, as summarized in Fig. 6(b). For *E. coli*, the inhibition zones of CCMP measured 15.40 ± 0.28, 13.75 ± 0.49, 16.5 ± 0.03, and 18.00 ± 1.68 mm, respectively. For *S. aureus*, the corresponding values were 16.35 ± 0.85, 17.92 ± 0.58, 32.82 ± 2.54, and 18.13 ± 0.59 mm, respectively. Collectively, these results underscored the influence of PDA and CMCS on the system's antibacterial behavior. All CCMP samples produced inhibition zones exceeding 13 mm, involving a

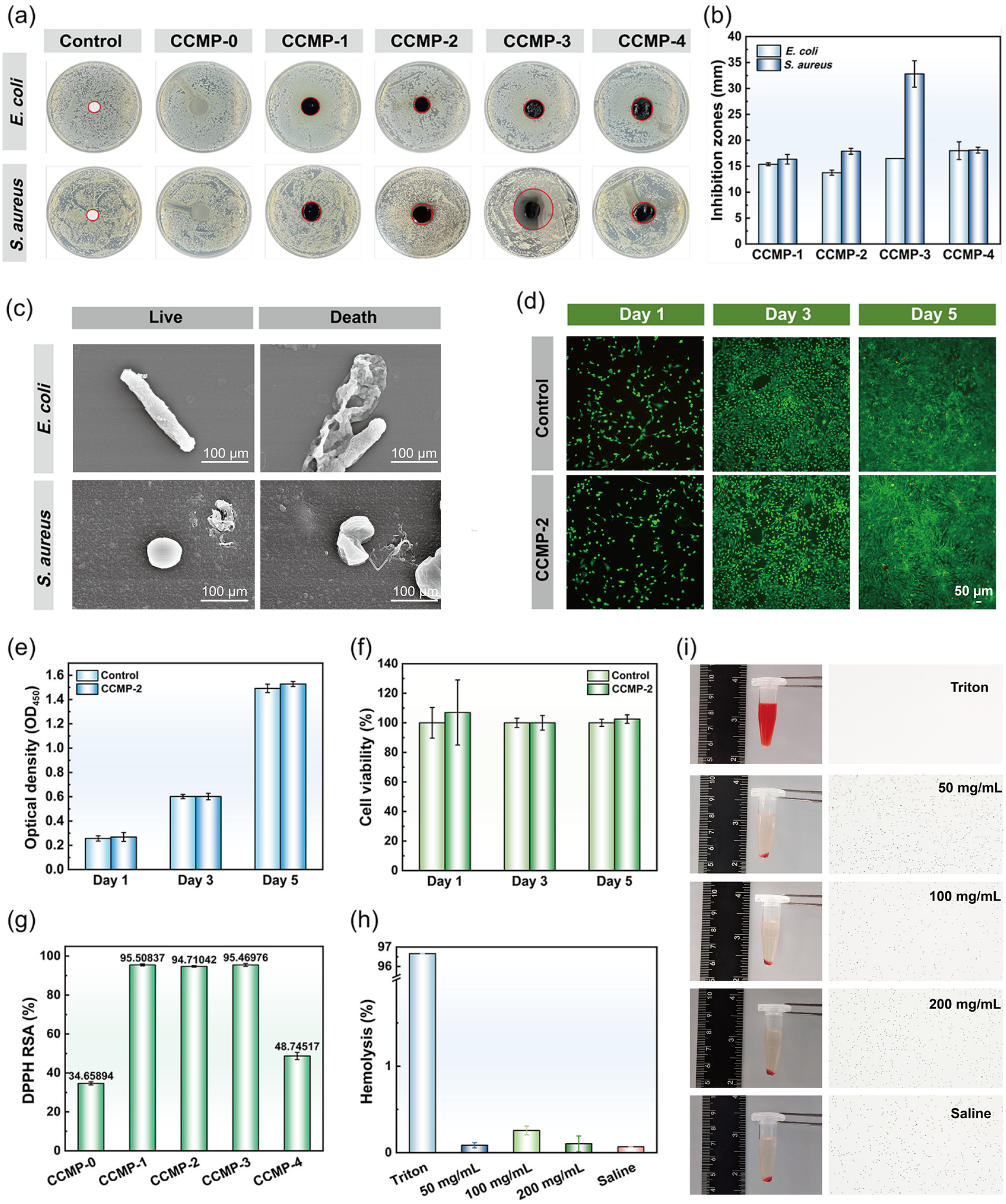

Figure 6 *In vitro* antibacterial properties and cytotoxicity of CCMP. (a) Optical image of the inhibition zone of CCMP on *E. coli* and *S. aureus*. (b) The diameter of inhibition zone of CCMP on *E. coli* and *S. aureus*. (c) SEM images reflecting the state of bacteria. (d) Live/dead staining images of different groups membrane CHL cells cultured for 1, 3, 5 days (scale bar: 50 μm). (e) Optical density and (f) cell viability of different groups on days 1, 3, 5. (g) DPPH free radical scavenging rate. (h) Hemolysis rate of CCMP-3. (i) Hemolysis experiment of CCMP-3 optical images and morphology of red blood cells were observed under a microscope.

maximum of 35 mm, confirming their excellent antibacterial performance. To further investigate the antibacterial mechanism, CCMP samples were immersed in bacterial solutions and incubated for 24 h. The bacteria were then fixed with 2.5% glutaraldehyde solution (pH 7.2) for 4 h and observed using field emission SEM. As shown in Fig. 6(c), bacteria without CCMP treatment displayed smooth, intact surfaces, indicating good viability. In contrast, those co-cultured with CCMP showed significant structural damage, including surface wrinkling and rupture, confirming loss of viability and further demonstrating the material's strong antibacterial activity. In summary, the results indicate that the multimodal conductive e-skin patch developed in this study possesses efficient antibacterial properties, providing a foundation for its application in green and safe health care.

The Cell Counting Kit-8 (CCK-8) assay was used to assess the cytotoxicity of CCMP at the cellular level. Figure 6(d) presents live/dead staining images of Chinese hamster lung (CHL) cells treated with CCMP-2 after 1, 3, and 5 days of culture, observed under a fluorescence microscope. Green and red fluorescence indicate live and dead hamster lung cells, respectively; the scale bar represents 50 μm. CCMP-2 was chosen for biocompatibility characterization because its higher MWCNTs-NH_2 content is more conducive to assessing cytocompatibility after nanocomponent introduction, which is a key prerequisite for ensuring the biosafety of electronic skin. Compared with the control group, the experimental groups showed no significant reduction in live cell count or increase in dead cells, confirming the good biocompatibility of the prepared multimodal conductive e-skin patch [48]. As shown in Figs. 6(e) and 6(f), the cell viability after 1, 3, and 5 days of incubation with CCMP-2 extract remained close to 100%, consistent with the control group. These results further demonstrate the favorable biocompatibility of CCMP. The material can be attached to the skin for extended periods without inducing inflammation or immune rejection, highlighting its strong potential for applications in continuous health monitoring and natural human–computer interaction.

Antioxidant activity plays a critical role in wound healing. An excess of free radicals can impede the healing process; therefore, electronic skin with free radical scavenging capabilities can significantly enhance wound repair by eliminating excessive reactive oxygen species (ROS) [49]. In this study, the free radical scavenging ability was evaluated using 2,2-diphenyl-1-picrylhydrazyl (DPPH) assay. As shown in Fig. 6(g), the flexible electronic skin CCMP demonstrates excellent antioxidant performance, with DPPH radical scavenging rates of 36.66%, 95.50%, 94.71%, 95.47%, and 48.75%, respectively. Among these, CCMP-1, CCMP-2, and CCMP-3 exhibit particularly strong antioxidant activity, each exceeding 95%. This high antioxidant performance can likely be attributed to a multifunctional antioxidant network formed through the synergistic interaction between DA and MWCNTs-NH_2. The catechol groups in DA covalently bind with MWCNTs-NH_2, enabling stable and efficient radical scavenging. Meanwhile, DA polymerizes into PDA, which is rich in quinone and phenolic hydroxyl groups that continuously neutralize ROS, thereby significantly enhancing the antioxidant capacity of the system [50]. These findings offer a promising new strategy for designing antioxidant electronic patches suitable for chronic wound management.

In this study, the hemolysis rate was measured to assess the blood compatibility of the flexible electronic patch, particularly its potential to cause red blood cell rupture (hemolysis). As shown in Fig. 6(h), the hemolysis rates of CCMP-3 samples across different concentration gradients were all below 1% and close to 0%. Compared with the control group, these results indicate extremely low hemolytic activity of the CCMP-3 samples, suggesting that they will not induce red blood cell rupture in blood during wound management applications—an effect that appears independent of sample concentration [51]. Furthermore, optical images from the hemolysis assay of CCMP-3 and microscopic images of red blood cell morphology (Fig. 6(i)) clearly show that cells treated with Triton X-100 turned bright red due to hemoglobin release. In contrast, both the CCMP-3 samples at various concentrations and the negative control group remained colorless, with no ruptured red blood cells observed under microscopy. These findings confirm the material's excellent blood compatibility. In summary, the electronic patch developed in this study is suitable for biological contact, underscoring its strong potential for use in wound management and other applications involving tissue interfaces.

3.7 Wound healing performance

Based on the demonstrated antibacterial and antioxidant properties from the *in vitro* biosafety studies, a 6 mm diameter full-thickness rat wound model was hereby utilized to assess the skin regeneration capacity, specifically, the wound healing performance of CCMP (Fig. 7) [43]. Figure 7(a) outlines the procedure and timeline for full-thickness wound treatment. Full-thickness skin defects were surgically created on the backs of rats and treated with CCMP-3 over a 14-day period. The animals were divided into three groups: the untreated blank control group, the CCMP-3 treatment group, and the commercial hydrogel negative control group. Wound images were captured on days 0, 3, 7, 10, and 14, while wound closure trajectories were simulated for each group across varying time points to quantify the wound closure rate (see Fig. 7(b)). Macroscopic evaluation revealed the most effective wound healing of the CCMP-3 group. Owing to its high water absorption capacity, CCMP effectively absorbed wound exudate, reduced localized tension, and maintained a dry wound surface. Furthermore, its favorable hydrophobic properties resulted in minimal adhesion to surface substances, thereby providing contamination resistance and protecting the wound from external pollutants [52]. Throughout the treatment period, body weight changes were recorded for mice in both the CCMP-3 and negative control groups. All animals exhibited a mild increasing trend in body weight over time (Fig. 7(c)). Additionally, we visualized the wound area and healing rate across different groups during the treatment. Figures 7(d) and 7(e) present the corresponding healing rates and a heat map of wound areas, respectively. Quantitative analysis indicated pronounced wound contraction at the edges in the CCMP-3 group by day 7. Compared to the other groups, the CCMP-3 group showed the least scar formation and achieved the highest healing rate of 98.21% by day 14 [53]. Histological evaluation of skin wounds at day 14 demonstrated that CCMP-3 treatment promoted complete re-epithelialization and granulation tissue formation (Fig. 7(f)). The nascent epidermis was well-defined and tightly integrated with the underlying granulation tissue, indicative of an advanced remodeling phase. In contrast, both control groups showed impaired healing, characterized by noticeable epidermal discontinuities and poor adhesion between the new epidermis and granulation tissue. Furthermore, wounds treated with the CCMP-3 e-skin patch exhibited superior architectural restoration and a

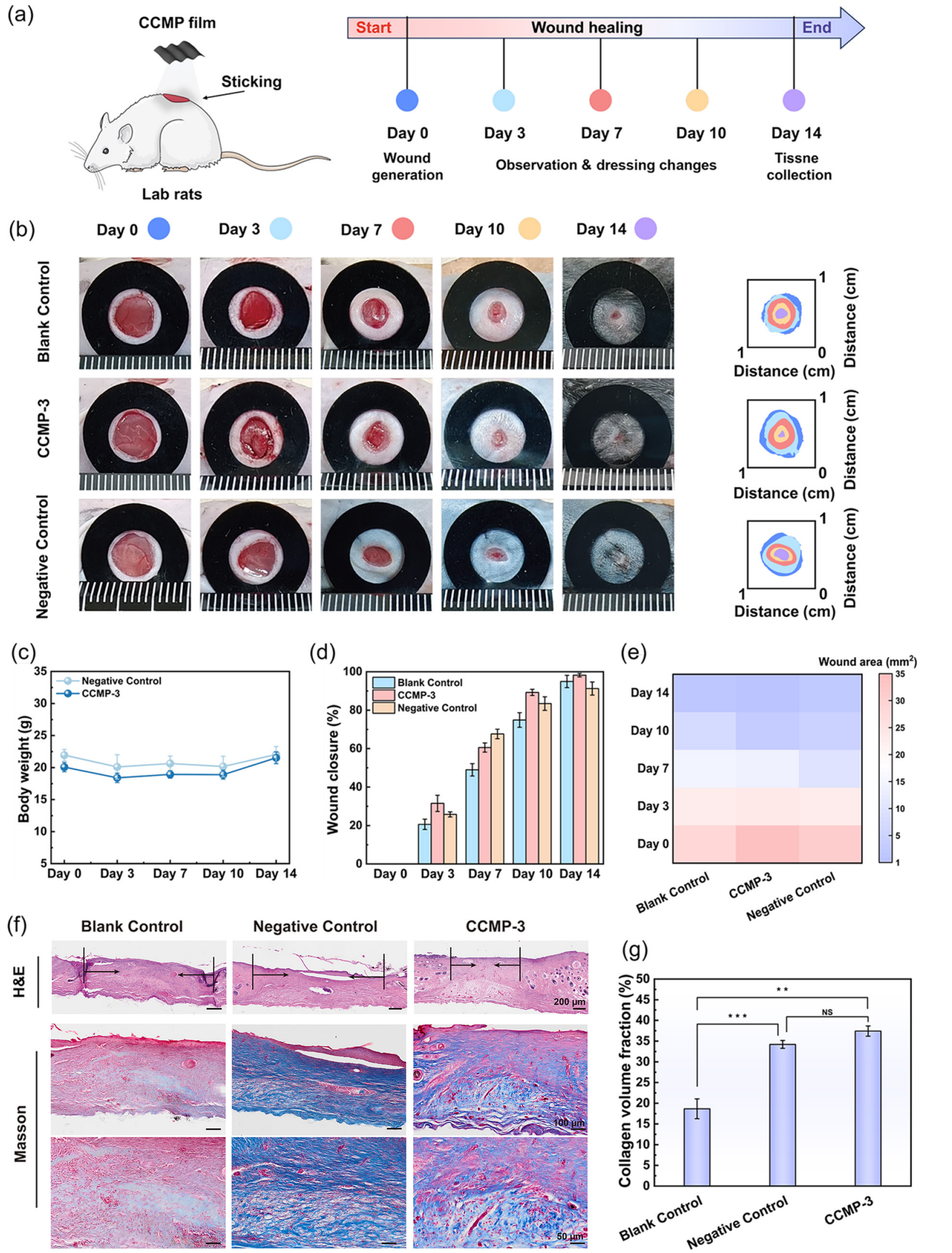

Figure 7 CCMP promotes wound healing in mice. (a) A schematic diagram and timeline of the healing process of full-thickness dermal wounds. (b) Representative optical images of wounds during 1–14 days of treatment and simulated wound closure trajectories at different time points in each group. (c) Changes in body weight of mice during treatment. (d) Wound healing rate of different groups during treatment. (e) Heat map of wound area in different groups during treatment. (f) H&E tissue staining and Masson staining images of different groups of wounds after 14 days of treatment. (g) Collagen volume fraction in different groups after 14 days of treatment.

significantly reduced wound width compared to the controls [54]. Masson staining further corroborated significant extracellular matrix remodeling in the CCMP-3 group, characterized by densely organized collagen fibers. Quantitative analysis confirmed a markedly higher collagen deposition compared to other groups (Fig. 7(g)). Collectively, these results demonstrate that the CCMP-3 e-skin patch exerts multifaceted therapeutic efficacy in wound treatment. It provides antibacterial protection while simultaneously absorbing exudate, thereby mitigating infection. Furthermore, it promotes tissue repair through its inherent antioxidant capacity.

3.8 Anti-inflammatory and angiogenesis effects

An imbalance between inflammatory cytokines and growth factors perturbs the healing process by prolonging inflammation and impeding the subsequent proliferative phase. To substantiate the impact of our e-skin patch on this process, we performed systematic immunohistochemical analyses to evaluate its anti-inflammatory and pro-angiogenic effects. The choice of CCMP-3 for wound healing experiments gave the material better antioxidant activity and anti-inflammatory potential because of its higher dopamine content, which has a direct and important regulatory effect on the actual wound healing process. In this study, tumor necrosis factor-alpha (TNF-α) was selected as an inflammatory marker and co-detected with the vascular regeneration markers cluster of differentiation 31 (CD31) and alpha-smooth muscle actin (α-SMA) via immunohistochemistry. This combined analysis provides key insights into the tissue microenvironment, specifically regarding inflammation, angiogenesis, and tissue remodeling (Fig. 8). The anti-inflammatory effects of CCMP may stem from the synergistic mechanism of its components: CMCS can regulate the immune response and inhibit the expression of pro-inflammatory factors; PDA scavenges reactive oxygen species through strong antioxidant activity and alleviates oxidative stress-related inflammatory responses. MWCNTs-NH_2 help maintain material stability and help improve the cellular microenvironment. In addition, CCMP's ultra-high swelling properties can quickly absorb wound exudate, and its antibacterial properties can also reduce inflammation caused by infection. As shown in Figs. 8(a) and 8(b), the expression of the pro-inflammatory cytokine TNF-α (red fluorescence) in the CCMP-3 treated wounds was significantly lower than that in both the negative and blank control groups after 14 days of treatment. Quantitative analysis confirmed this marked reduction, indicating that the CCMP e-skin patch effectively attenuated the inflammatory response. Collectively, our findings

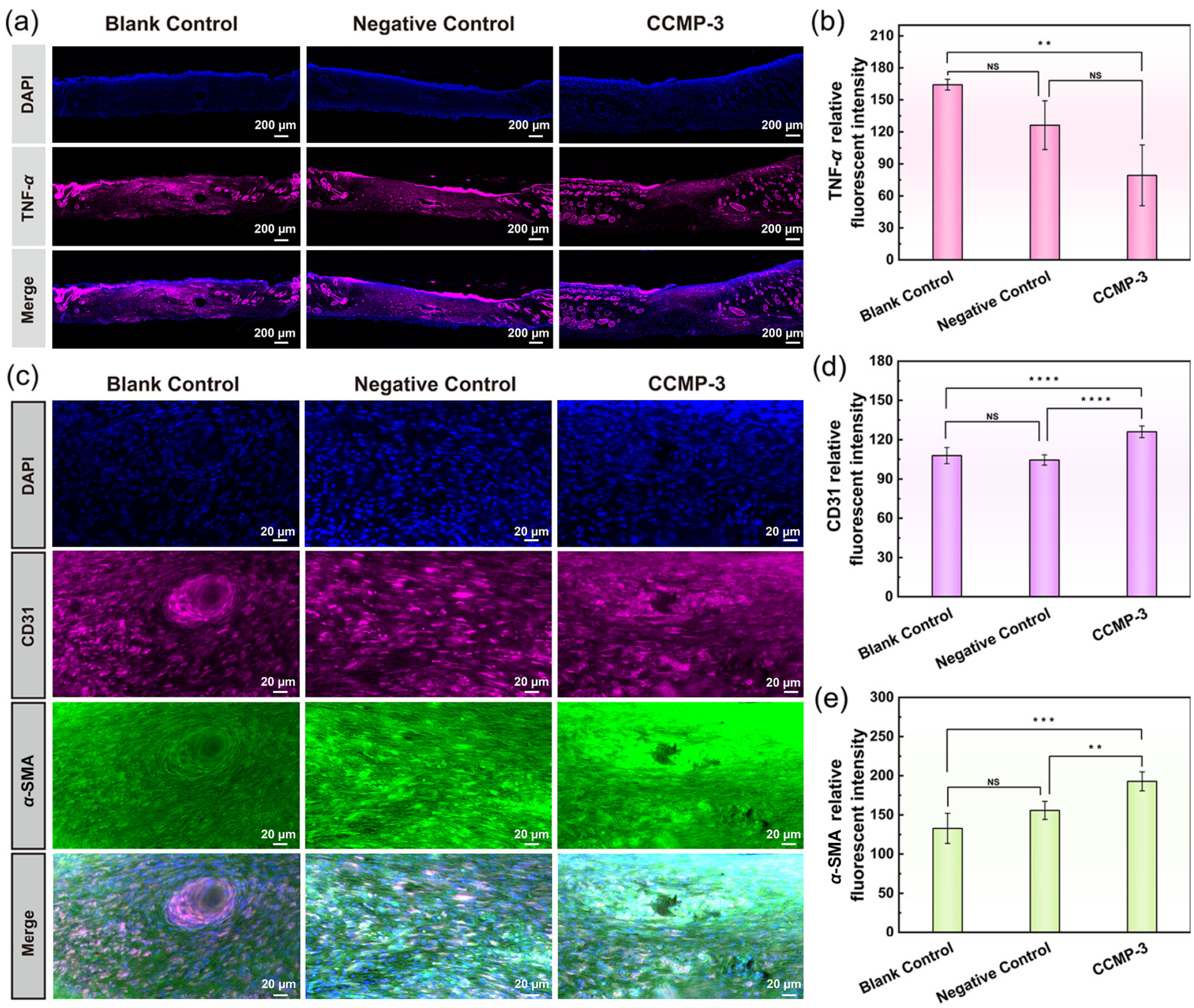

Figure 8 Anti-inflammatory and angiogenesis effects of CCMP. (a) Immunohistochemical detection of inflammatory factors TNF-α. (b) Quantitative analysis of TNF-α positive regions. (c) Immunohistochemistry of vascular regeneration factor CD31 and α-SMA. (d) Quantitative analysis of CD31-positive regions. (e) Quantitative analysis of α-SMA-positive regions.

demonstrate that the CCMP e-skin patch, via its inherent ROS-scavenging capability, modulates the anti-inflammatory response, which constitutes a key underlying mechanism for promoting wound healing. Angiogenesis was further verified using dual-color immunofluorescence for CD31 (red; endothelial cells) and α-SMA (green; vascular smooth muscle cells). The results in Figs. 8(c)–8(e) demonstrated a significant enhancement of vascularization in the CCMP-3 group, as quantified by the coverage areas of both CD31 and α-SMA. Consequently, a mature and functional vascular network was formed, providing critical support for the tissue regeneration process. The CCMP-3 group exhibited the highest percentage of CD31 and α-SMA positive areas, indicating enhanced neovascularization during the early healing phase [55]. Consistent with the aforementioned improved wound closure rate, this robust angiogenesis aligns with a controlled inflammatory response and the subsequent transition to a robust proliferative stage, characterized by healthy granulation tissue. These findings collectively underscore the considerable potential of the multimodal conductive CCMP e-skin patch in accelerating wound healing by effectively mitigating inflammation and promoting vascular regeneration. Furthermore, histopathological examination of major organs (heart, liver, spleen, lungs, and kidneys) revealed no evidence of structural abnormalities, cellular degeneration, apparent inflammatory lesions, or tissue damage in any of the mice (Fig. S6 in the ESM). Collectively, these findings corroborate the excellent biocompatibility and *in vivo* safety of the CCMP e-skin patch, thereby laying a solid foundation for its potential application in wound healing.

3.9 Strain sensing, physiological signal and motion monitoring

Its excellent mechanical properties and high electrical conductivity endowed CCMP with considerable potential as a strain sensor. Furthermore, wound-related impairments could compromise the skin's ability to perceive external stimuli. As an electronic patch, CCMP was expected to compensate for such temporary functional deficits by detecting electrical signal variations in response to dynamic mechanical changes [56]. To assess its performance and practical applicability, a series of comprehensive tests were hereby conducted on the stretchable strain sensor. Specifically, CCMP-2 (3 cm × 4 cm), exhibiting the highest conductivity, was selected for sensor fabrication. Copper wires were attached to both ends of the sample and connected to the electrodes of an electrochemical workstation. The sensor was then affixed to various parts of the human body to simulate monitoring of normal daily activities across multiple scenarios. Additionally, real-time motion signals were recorded under an applied voltage of 3 V. Figure 9(a) shows that the response/recovery time of the CCMP strain sensor is approximately 0.6 s, indicating its ability to rapidly respond to strain stimuli. This performance ensures that, when used as an electronic patch, the sensor can accurately and promptly capture physiological signals without distortion. Examples include micro-movements during wound healing—such as muscle contractions and joint bending—as well as abnormal swelling due to early-stage infections. Such capabilities provide a reliable dynamic data foundation for precise medical interventions. As illustrated in Figs. 9(b)–9(e) and Video S2 in the ESM, when attached to fingers, wrists, and elbows, the CCMP strain sensor effectively captures motion signals that reflect the degree of bending in each joint. This confirms the reliability of its sensing performance across varying strain levels. Additionally, the sensor can detect the speed of finger bending. The changes in $\Delta R/R_0$ shown in Figs. 9(b) and 9(c) allow clear distinction between different finger bending speeds. The signal output remains stable with minimal hysteresis, making the sensor well-suited for high-fidelity signal detection. Furthermore, Figs. 9(f) and 9(g) demonstrate that the sensor, when mounted on the sole of a shoe, successfully detects limb movements and collects kinematic information during activities such as walking and running. Each type of motion is recorded clearly, with continuous and stable signal output, highlighting the sensor's potential for applications in motor behavior monitoring. As depicted in Figs. 9(h) and 9(i), the CCMP sensor was attached inside a mask to monitor breathing activity while worn. The sensor successfully detected respiratory movements in real time, converting physiological breathing behavior into recordable, analyzable, and feedback-ready waveform data. A comparison of breathing patterns before and after exercise further confirmed the stability and accuracy of the real-time electrical signals output by the CCMP sensor. The ability to reliably monitor such subtle physiological activities highlights its potential for applications in preventive health care, such as tracking chronic respiratory conditions, personalized wellness, and human–machine integration [57]. As shown in Fig. 9(j), the sensor was also mounted on the larynx region of the neck. Here, the CCMP sensor demonstrated the ability to detect and accurately output signals corresponding to swallowing activity in real time, suggesting promising utility for speech recognition and vocal monitoring systems.

3.10 Temperature early warning devices

CCMP exhibited temperature-sensing functionality, enabling attachment to the skin surface for real-time temperature monitoring and early warning [58]. To evaluate the feasibility of CCMP as a temperature sensor, CCMP-2 (3 cm × 4 cm) with the highest conductivity was selected and connected to an electrochemical workstation. The sensor was attached to a temperature-controlled water bath beaker, and real-time resistance changes were recorded under a 3 V applied voltage. The collected data were fitted (R^2 = 0.9679) to facilitate calculation of the temperature coefficient of resistance (TCR) and the thermistor constant (B). As shown in Fig. 10(a), the electrical response of the CCMP temperature sensor exhibited a negative linear correlation with temperature over the range of 26–90 °C. As temperature increased, the resistance of the CCMP decreased gradually, with the response stabilizing between 70 and 90 °C. The temperature-sensing performance was further evaluated using TCR, with a larger |TCR| indicating higher sensitivity [59, 60]. As depicted in Fig. 10(b), the relative resistance change was monitored, and the TCR was calculated between 26 and 76 °C. The fabricated multimodal conductive e-skin patch demonstrated a broad thermal response range. Based on the fitted curve, the TCR values were −8.58%/°C, −5.26%/°C, and −2.21%/°C within the temperature intervals of 26–45, 45–60, and 60–76 °C, respectively. Further investigations were conducted on the variation of electrical resistance with temperature within the near-body temperature range (34–45 °C). As shown in Fig. 10(c), the fitted TCR value within this interval is −7.84%/°C, indicating that the sensor can accurately detect subtle temperature changes within a narrow range. A higher B value suggests that the thermistor exhibits a faster thermal response, rendering it more suitable for highly sensitive and precise temperature sensing applications. As depicted in Fig. 10(d), across the full span of 35–45 °C, the fitted B value of the

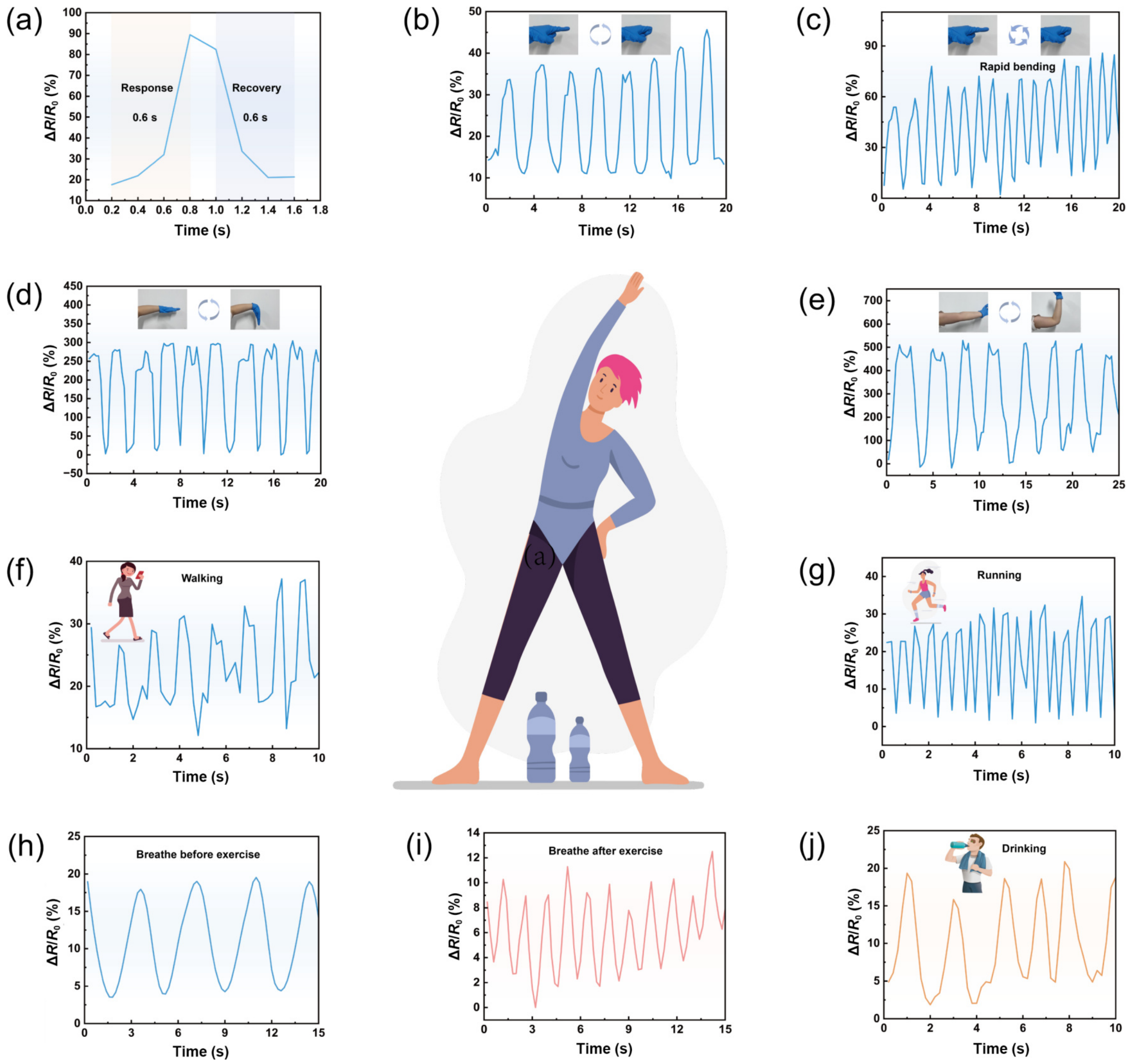

Figure 9 Pressure sensing performance of CCMP. (a) Response/recovery time of CCMP strain sensor. The change of relative resistance during (b) finger bending and (c) accelerated finger bending. The change of relative resistance when bending (d) wrist and (e) elbow. Changes in relative resistance during (f) walking and (g) running. Changes in relative resistance during breathing (h) before and (i) after exercise when wearing a mask. (j) The change of relative resistance when drinking water.

resistance–temperature characteristic for the CCMP thermistor is 2811.75 K (R^2 = 0.9998). Based on these findings, the CCMP temperature sensor developed in this work demonstrates high sensitivity (with a maximum TCR of −7.84%/°C) and a broad operational range (26–76 °C), highlighting its strong potential for use in multimodal conductive e-skin patches (CCMP) for body temperature monitoring. As illustrated in Fig. 10(e), the CCMP temperature sensor exhibits distinct and stable current curves at each temperature gradient, confirming its ability to function as a flexible wearable sensor that can be directly attached to human skin or curved surfaces for continuous and reliable temperature monitoring. To further evaluate its early warning capability, the CCMP temperature sensor was connected to an electrochemical workstation and placed in contact with the external surface of a beaker filled with water at different temperatures. Real-time resistance changes of the patch were accurately recorded (Fig. 10(f)). In another experiment (Fig. 10(g)), a CCMP-2 sample (1 cm × 2 cm) was attached to a model finger pad and connected to the electrochemical workstation (Video S3 in the ESM). As the water temperature increased to 30 °C, 40 °C, 50 °C, 60 °C, and 70 °C under an applied voltage of 3 V, the finger model was brought near the beaker for 15 s at each step, and corresponding resistance changes were measured. The relative resistance curves clearly show a decreasing trend in resistance under various thermal stimuli, confirming the sensor's ability to monitor temperature accurately and activate a warning function. Moreover, the resistance signal recovered quickly after each thermal stimulus was removed. In conclusion, these results underscore the potential of CCMP as an intelligent protective material suitable for temperature detection, scald prevention, and early fire warning.

3.11 Portable wireless wearable system

When monitoring wound healing, the status of recovery and the presence of inflammatory reactions can be assessed by monitoring local temperature and exudate level [61]. Compared to normal skin tissue, an increase in wound exudate (often linked to inflammation) generally causes the local temperature to rise by roughly 3.5 °C [62]. Herein, CCMP was integrated into a portable wireless wearable monitoring system designed for long-term tracking of physical activity and wound conditions to facilitate the diagnosis of wound infection [63]. As illustrated in Fig. 11(a), the system incorporated a

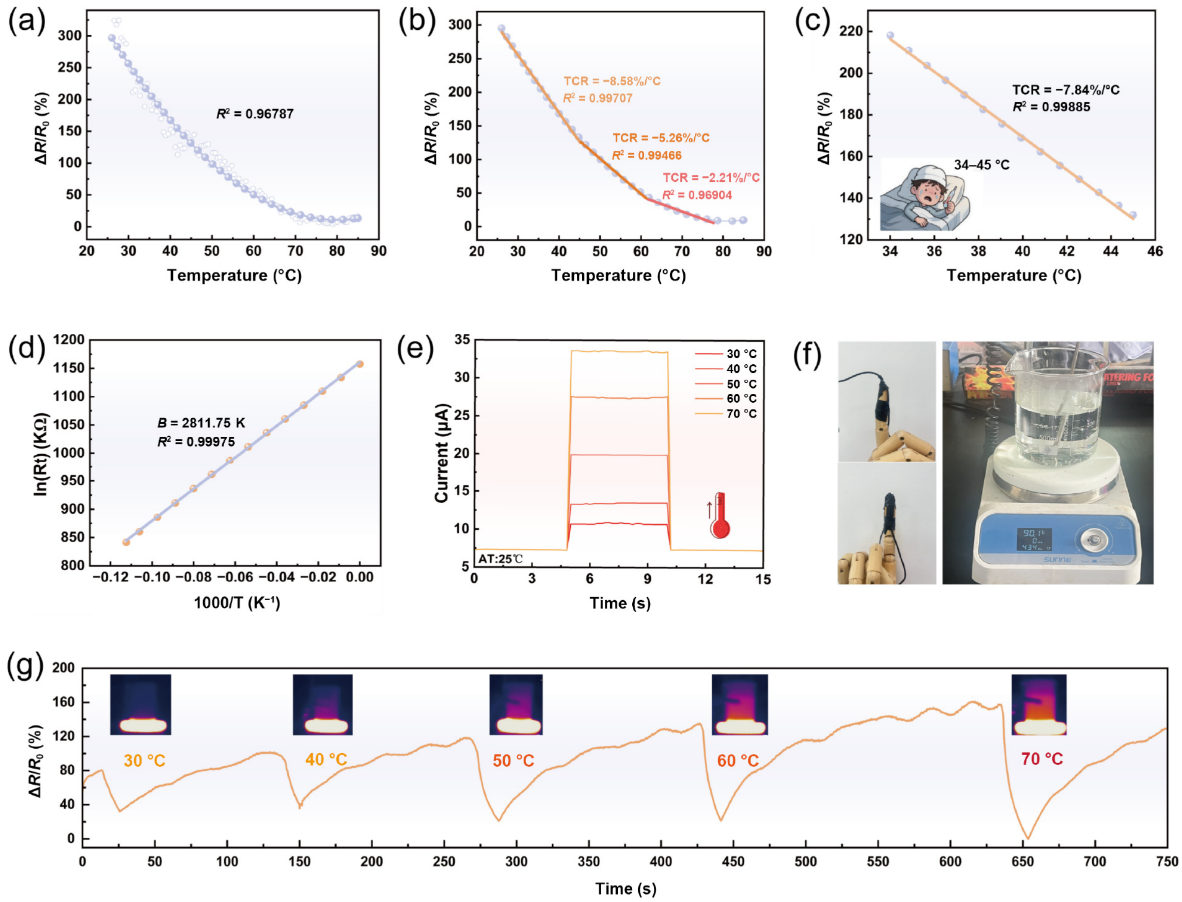

Figure 10 Temperature sensing performance of CCMP. (a) In the range of 26–90 °C, the relative resistance of the CCMP sensor changes with temperature. (b) In the range of 26–76 °C, the change of relative resistance with temperature and the corresponding fitted TCR value. (c) In the range of 34–45 °C, the change of relative resistance with temperature and the corresponding fitted TCR value. (d) The fitting results of thermistor constant. (e) The change of current with time under different temperature gradients. (f) Skin touch temperature alarm device diagram. (g) The temperature alarm curve of high-fidelity thermal sensation of biomass-based intelligent electronic fabrics at different temperatures was realized by using the heating table as the heat source.

custom-designed printed circuit board (PCB) circuit board equipped with a wireless ESP32 chip (supporting Wi-Fi and Bluetooth connectivity), an analog-to-digital converter (ADC), a low dropout linear regulator (LDO) linear regulator, a universal serial bus to transistor-transistor logic serial converter (USB-to-TTL) serial converter, and a power management module. Incorporating a Type-C interface allowed for convenient charging at any time [64]. Figure 11(b) presents a schematic diagram of the CCMP integrated with a portable wireless wearable module, along with its placement on the human body. The CCMP could be attached to various body parts or wound surfaces to support motion detection or wound management. As shown in Fig. 11(c) and Video S4 in the ESM, the entire system can be wirelessly controlled via terminal devices such as smartphones and computers. By incorporating both strain and temperature sensing functions, the CCMP e-skin patch enables real-time monitoring of mechanical deformations (e.g., stretching and compression) and local temperature variations at the wound site. The collected data are transmitted wirelessly to medical terminals or patients' mobile devices. Dynamic trends in the real-time data can be analyzed to trigger timely early warnings. The strain sensor captures tissue contractions or abnormal activity during wound healing, while the temperature sensor detects signs of infection such as redness, swelling, heat, and pain associated with elevated temperature. This system provides medical staff with accurate data to support wound assessment and helps guide patients to adjust self-care behaviors—such as reducing physical activity or seeking prompt medical attention—thereby facilitating optimized, personalized wound management. The CCMP was mounted on a glass rod to function as an E-pen, and the arbitrary digits "0 2 0 7" were written to validate its strain-sensing performance and demonstrate its feasibility as an electronic pen (Video S5 in the ESM) [6]. Additionally, the CCMP was attached to various parts of the human body or wound surfaces to form an electronic patch (E-patch) capable of real-time data transmission. As shown in Fig. 11(d) and Table S4 in the ESM, a comparison is provided between the CCMP and previously reported e-skin patches [6, 10, 35, 65–71]. Figure 11(e) further illustrates the application potential of the CCMP. For instance, it can be used to regulate patients' body temperature and facilitate multimodal intelligent responses such as wound healing and antibacterial effects, which contribute positively to wound recovery (WHR = 98.21%). It also shows significant promise in motion monitoring, enabling real-time recording and transmission of kinematic data. Moreover, in high-temperature environments, the CCMP can serve as a temperature warning system by effectively monitoring thermal changes and detecting anomalies in a timely manner, thereby enhancing safety across various application scenarios.

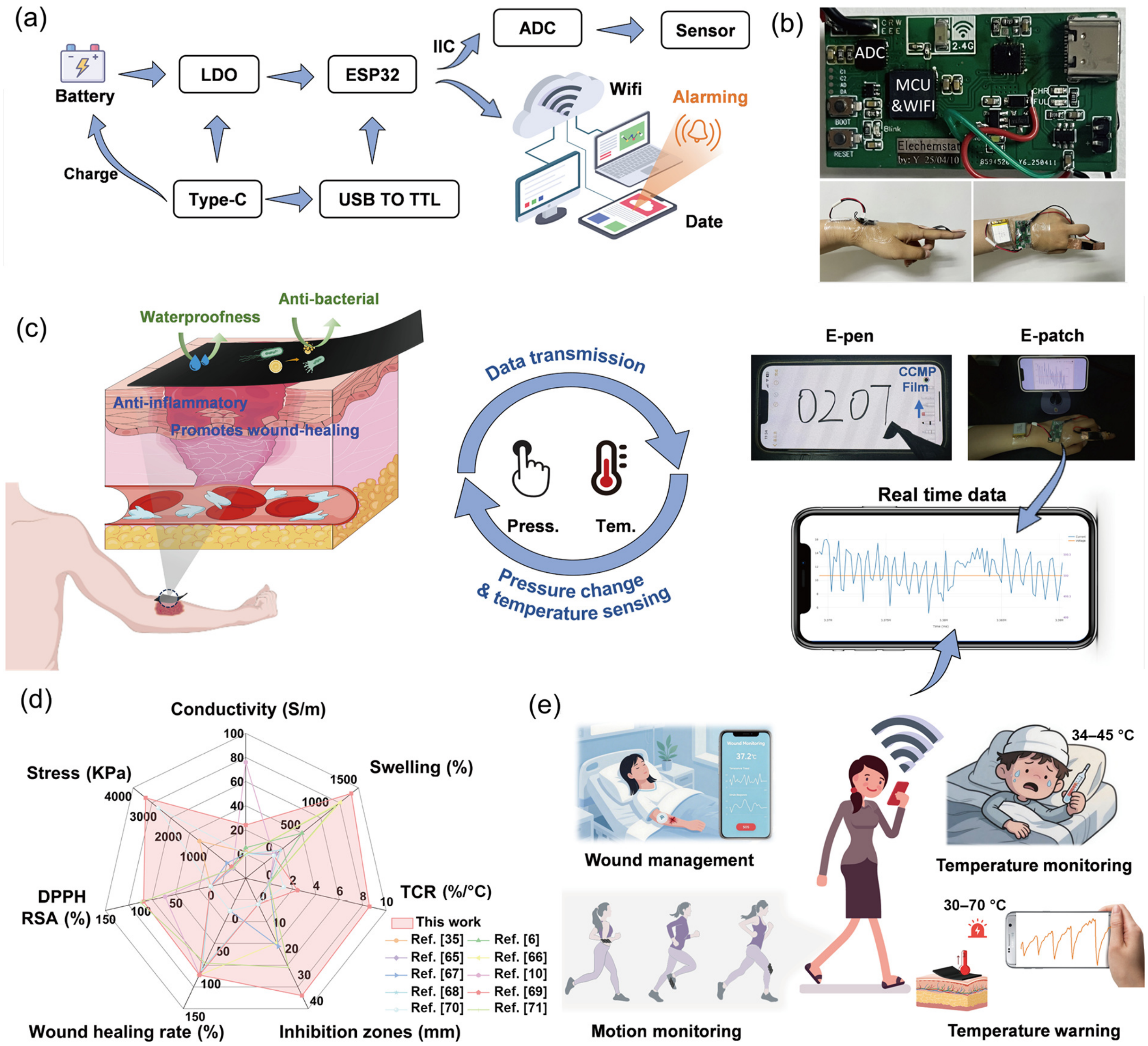

Figure 11 Portable wireless wearable system based on CCMP. (a) Portable wireless wearable module system block diagram. (b) The physical diagram of the CCMP integrated with the portable wireless wearable module and the schematic diagram of the wireless wearable module carried by the human body. (c) The application mechanism of CCMP integrated with portable wireless wearable module. (d) Comparison of CCMP with previously reported e-skin patches. (e) The application scenario of CCMP integrated with portable wireless wearable module.

4 Conclusions

In this study, a natural biomass-derived CCMP was developed based on natural biomass resources (CMS and CMCS). Specifically, the CCMP was fabricated by incorporating MWCNTs-NH_2 and DA into a CMS/CMCS/PVA matrix via supramolecular assembly. The CCMP synergistically integrated personal thermal management (PTM), human health sensing, and real-time wound-status monitoring and treatment. The fabricated CCMP exhibited high electrical conductivity (24.1 S/m), efficient photothermal conversion (with a heating time constant τ_s = 66.66 s), strong antioxidant activity (> 95.50%), effective antibacterial performance (inhibition zone diameter up to 35 mm), hydrophobicity (water contact angle up to 108°), electromagnetic shielding capability, as well as high sensitivity to temperature (TCR = −8.58%/°C), strain, and electrical signals. Furthermore, the CCMP also demonstrated ultra-high swelling properties: water sorption reached 1374%, swelling ratio was 437%, and simulated body fluid absorption stood at 384%. As an e-skin patch, this enabled rapid wound exudate absorption while maintaining an optimally moist environment, making it particularly suitable for managing highly exuding wounds. Additionally, the e-skin patch sensor could also be integrated with a miniaturized electronic chip to form a portable wireless wearable system. At present, there are still experimental models that are more idealistic and have not yet covered the limitations of complex clinical scenarios (such as infected wounds and chronic ulcers). In the future, large animal experiments and prospective clinical research should be carried out to promote translational applications. To conclude, this natural biomass-derived smart e-skin patch offers unique advantages and represents a powerful non-invasive solution for comprehensive wound repair and real-time wound-status monitoring and treatment.

Electronic Supplementary Material: Supplementary material (characterization measurements of multimodal conductive e-skin patch (CCMP) (FTIR, XRD, XPS, thermogravimetric analysis, surface morphology, mechanical properties, light transmittance, tailorability, conductivity, and swelling behavior), electromagnetic shielding performance, photothermal conversion performance, antimicrobial properties, biocompatibility, antioxidant properties, hemolytic property, wound healing performance, multimodal sensing performance, portable wireless wearable system, Tables S1–S4, and Figs. S1–S6) is available in the online version of this article at https://doi.org/10.26599/NR.2026.94908706.

Data availability

All data needed to support the conclusions in the paper are presented in the manuscript and/or the Electronic Supplementary Material. Additional data related to this paper may be requested from the corresponding author upon request.

Acknowledgements

This research was financially supported by the Shaanxi Provincial Department of Education Scientific Research Program (No. 25JC016), "Scientists + Engineers" Talent Team Construction Project of Xianyang City (No. L2024-CXNL-KJRCTD-DWJS-0003), and Shandong province key research and development plan—project for enhancing the innovation capability of technology-based small and medium-sized enterprises (No. 2025TSGCCZZB0018).

Declaration of competing interest

All the contributing authors report no conflict of interests in this work.

Author contribution statement

X. G. D.: Data curation, validation, writing manuscript, experimental design, funding acquisition. Y. F. F.: Data curation, validation, experimental design, writing manuscript. H. J. W.: Data curation, writing manuscript. X. C. W.: Data curation. M. Y. T.: Data curation, validation. M. H. Z.: Data curation, validation. All the authors have approved the final manuscript.

Informed consent

Not applicable.

Ethics statement

The animal experiments were carried out following the guidelines of the Animal Ethics Committee of Wenzhou Medical University and were approved by the Committee on Ethical Use of Animals of Wenzhou Medical University (Ethics code: wydw2025-0083).

Use of AI statement

None.

References

[1] Lee, J. H.; Cho, K.; Kim, J. K. Age of flexible electronics: Emerging trends in soft multifunctional sensors. *Adv. Mater.* **2024**, *36*, 2310505.

[2] Wang, Z.; Hu, Q. H.; Yao, S. C.; Wang, S. B.; Liu, X.; Zhang, C. P.; Wang, Z. L.; Li, L. L. Flexible triboelectric nanogenerator patch for accelerated wound healing through the synergy of electrostimulation and photothermal effect. *Small* **2025**, *21*, 2409756.

[3] Fu, X. M.; Cheng, W.; Wan, G. X.; Yang, Z. J.; Tee, B. C. K. Toward an AI era: Advances in electronic skins. *Chem. Rev.* **2024**, *124*, 9899–9948.

[4] Chen, K.; Liang, K. W.; Liu, H.; Liu, R. N.; Liu, Y. U.; Zeng, S. J.; Tian, Y. Skin-inspired ultra-tough supramolecular multifunctional hydrogel electronic skin for human-machine interaction. *Nano-Micro Lett.* **2023**, *15*, 102.

[5] Yue, O. Y.; Wang, X. C.; Hou, M. D.; Zheng, M. H.; Bai, Z. X.; Cui, B. Q.; Cha, S. Y.; Liu, X. H. Skin-inspired wearable self-powered electronic skin with tunable sensitivity for real-time monitoring of sleep quality. *Nano Energy* **2022**, *91*, 106682.

[6] Kim, H.; Dutta, S. D.; Jeon, M. J.; Lee, J.; Park, H.; Seol, Y.; Lim, K. T. Bioinspired shape reconfigurable, printable, and conductive "E-skin" patch with robust antibacterial properties for human health sensing. *Adv. Funct. Mater.* **2025**, *35*, 2504088.

[7] Li, J. Y.; Wang, H.; Luo, Y. B.; Zhou, Z. J.; Zhang, H.; Chen, H. Z.; Tao, K.; Liu, C.; Zeng, L. X.; Huo, F. W. et al. Design of AI-enhanced and hardware-supported multimodal E-skin for environmental object recognition and wireless toxic gas alarm. *Nano-Micro Lett.* **2024**, *16*, 256.

[8] Duan, S. S.; Shi, Q. F.; Hong, J. L.; Zhu, D.; Lin, Y. C.; Li, Y. H.; Lei, W.; Lee, C.; Wu, J. Water-modulated biomimetic hyper-attribute-gel electronic skin for robotics and skin-attachable wearables. *ACS Nano* **2023**, *17*, 1355–1371.

[9] Chen, C.; Xu, J. L.; Wang, Q.; Li, X. L.; Xu, F. Q.; Gao, Y. C.; Zhu, Y. B.; Wu, H. A.; Liu, J. W. Biomimetic multimodal receptors for comprehensive artificial human somatosensory system. *Adv. Mater.* **2024**, *36*, 2313228.

[10] Jia, Z. R.; Gong, J. L.; Zeng, Y.; Ran, J. H.; Liu, J.; Wang, K. F.; Xie, C. M.; Lu, X.; Wang, J. Bioinspired conductive silk microfiber integrated bioelectronic for diagnosis and wound healing in diabetes. *Adv. Funct. Mater.* **2021**, *31*, 2010461.

[11] Cai, X. X.; Wang, X. Q.; Bian, F. P.; Li, J. Y.; Zhou, R. X.; Hu, J. W.; Lin, S. D. Flexible sensor based on conformable, sticky, transparent elastomers for electronic skin. *Chem. Eng. J.* **2024**, *498*, 154934.

[12] Liu, X. Y. The more and less of electronic-skin sensors. *Science* **2020**, *370*, 910–911.

[13] Wang, L.; Ren, W. N.; Hu, X. F.; He, M. K.; Men, J.; Guo, H.; Zhang, Y. L.; Shi, X. T.; Qiu, H.; Ji, X. H. Biomass materials and their derivatives for electromagnetic interference shielding: A review. *J. Mater. Sci. Technol.* **2026**, *243*, 28–44.

[14] Su, Z. P.; Yang, Y.; Huang, Q. B.; Chen, R. W.; Ge, W. J.; Fang, Z. Q.; Huang, F.; Wang, X. H. Designed biomass materials for "green" electronics: A review of materials, fabrications, devices, and perspectives. *Prog. Mater Sci.* **2022**, *125*, 100917.

[15] Li, N. N.; Qin, H.; Tang, Q.; Peng, D. J.; Luo, X. Y.; Li, H. P.; Zou, Z. M. Development and application of intelligent packaging films based on carboxymethyl starch/PVA with Cu-LTE nanocrystal as functional compatibilizer. *Food Packag. Shelf Life* **2024**, *43*, 101306.

[16] Yang, Y. H.; Wei, Z. J.; Hu, S. L.; Tang, B.; Qu, G. M.; Yue, C. C.; Li, X. M.; Han, C. P. Ion redistribution gel electrolyte dissipates interfacial turbulence for aqueous zinc-ion batteries. *Adv. Energy Mater.* **2025**, *15*, 2404367.

[17] Pooresmaeil, M.; Namazi, H. Developments on carboxymethyl starch-based smart systems as promising drug carriers: A review. *Carbohydr. Polym.* **2021**, *258*, 117654.

[18] Zhao, K.; Guo, Z. X.; Wang, J. F.; Xie, H. Q. Construction of phase change n-Octadecane microencapsulated in carbon nanotubes-modified polymer for thermal management applications of finned heat sinks. *Chem. Eng. J.* **2023**, *471*, 144723.

[19] Hsiao, L. Y.; Jing, L.; Li, K. R.; Yang, H. T.; Li, Y.; Chen, P. Y. Carbon nanotube-integrated conductive hydrogels as multifunctional robotic skin. *Carbon* **2020**, *161*, 784–793.

[20] Lu, Y. Y.; Li, X. T.; Compton, R. G. Electro-oxidation of amino-functionalized multiwalled carbon nanotubes. *Chem. Sci.* **2022**, *13*, 1355–1366.

[21] Wan, S.; Deng, T. T.; Song, Q. F.; Bai, X. D.; Liu, Z. P.; Qiu, P. F.; Wei, T. R.; Shi, X. Enhanced thermoelectric performance in $Cu_7Sn_3S_{10}$-based hybrid materials with highly dispersed multiwalled carbon nanotubes. *Adv. Funct. Mater.* **2025**, *35*, 2505141.

[22] Wan, B. L.; Liu, N. N.; Zhang, Z.; Fang, X.; Ding, Y. G.; Xiang, H. S.; He, Y. Q.; Liu, M. X.; Lin, X. M.; Tang, J. T. et al. Water-dispersible and stable polydopamine coated cellulose nanocrystal-MXene composites for high transparent, adhesive and conductive hydrogels. *Carbohydr. Polym.* **2023**, *314*, 120929.

[23] Gong, X. H.; Luo, Y.; Zhang, C. Q.; Xie, J. T.; Wang, Y. Carboxymethyl chitosan-based tough hydrogels with low mechanical hysteresis and high conductivity as multifunctional sensors. *Chem. Eng. J.* **2025**, *510*, 161610.

[24] Peng, X.; Dong, K.; Zhang, Y. F.; Wang, L. L.; Wei, C. H.; Lv, T. M.; Wang, Z. L.; Wu, Z. Y. Sweat-permeable, biodegradable, transparent and self-powered chitosan-based electronic skin with ultrathin elastic gold nanofibers. *Adv. Funct. Mater.* **2022**, *32*, 2112241.

[25] Liang, Y. P.; He, J. H.; Guo, B. L. Functional hydrogels as wound dressing to enhance wound healing. *ACS Nano* **2021**, *15*, 12687–12722.

[26] Chang, G. Z.; Dang, Q. F.; Liu, C. S.; Wang, X. Y.; Song, H.; Gao, H.; Sun, H. T.; Zhang, B. N.; Cha, D. S. Carboxymethyl chitosan and carboxymethyl cellulose based self-healing hydrogel for accelerating diabetic wound healing. *Carbohydr. Polym.* **2022**, *292*, 119687.

[27] Zhang, P. F.; Wang, W. W.; Ma, Y. H.; Zhang, H.; Zhou, D. D.; Ji, X. Y.; Liu, W. Z.; Liu, Y. K.; Zhang, D. Z. MXene-based self-adhesive, ultrasensitive, highly tough flexible hydrogel pressure sensors for motion monitoring and robotic tactile sensing. *Chem. Eng. J.* **2024**, *499*, 156173.

[28] Lu, C. W.; Xu, S. J.; Tang, D. P.; Huang, C. X.; Zhang, D. H.; Gao, S. S.; Wang, J. F.; Wang, C. P.; Yong, Q.; Chu, F. X. Cellulose-enabled dynamic crosslinking microdomains strategy inducing high strong and tough, reprocessable bio-elastomer for durable self-powered electronic textiles. *Chem. Eng. J.* **2025**, *508*, 161024.

[29] Ren, J.; Yang, X.; Xiang, X. Carboxymethyl cellulose-reinforced sandwich-structured carbon nanotube composite hydrogels for strain sensing and joule heating. *Carbohydr. Polym.* **2025**, *369*, 124291.

[30] Li, X. M.; Wu, Z. Z.; Zhang, B.; Pan, Y.; Meng, R.; Chen, H. Q. Fabrication of chitosan hydrochloride and carboxymethyl starch complex nanogels as potential delivery vehicles for curcumin. *Food Chem.* **2019**, *293*, 197–203.

[31] Luo, X. Y.; Wang, S.; Wu, N.; Zhang, L.; He, Q. C.; Ren, L. L.; Song, W. Dual-network conductive hydrogels based on carboxymethylcellulose/ aminated carbon nanotube reinforcement: Monitoring human micro-expressions and signal changes. *Int. J. Biol. Macromol.* **2025**, *320*, 146012.

[32] Zahib, I. R.; Md Tahir, P.; Talib, M.; Mohamad, R.; Alias, A. H.; Lee, S. H. Effects of degree of substitution and irradiation doses on the properties of hydrogel prepared from carboxymethyl-sago starch and polyethylene glycol. *Carbohydr. Polym.* **2021**, *252*, 117224.

[33] Dang, X. G.; Yu, Z. F.; Yang, M.; Woo, M. W.; Song, Y. Q.; Wang, X. C.; Zhang, H. J. Sustainable electrochemical synthesis of natural starch-based biomass adsorbent with ultrahigh adsorption capacity for Cr(VI) and dyes removal. *Sep. Purif. Technol.* **2022**, *288*, 120668.

[34] Ding, S. S.; Jin, X.; Guo, J.; Kou, B. X.; Chai, M. Y.; Dou, S.; Jin, G. L.; Zhang, H. J.; Zhao, X. M.; Ma, J. Y. et al. A biomimetic asymmetric structured intelligent wound dressing with dual-modality humidity-pressure sensing for non-invasive and real-time wound healing monitoring. *Adv. Fiber Mater.* **2025**, *7*, 156–171.

[35] Wang, H. Y.; Han, P.; Yu, Y.; Han, S. L.; Qiao, Y.; Li, Y. H.; Sun, B.; Gu, Z. Multifunctional flexible MXene/TA@CNC electronic hydrogel patch with robust adhesion and self-healing properties for wearable electronics. *Chem. Eng. J.* **2025**, *507*, 160329.

[36] Zhang, C. J.; Chi, W. R.; Meng, F. S.; Wang, L. J. Fabricating an anti-shrinking κ-carrageenan/sodium carboxymethyl starch film by incorporating carboxylated cellulose nanofibrils for fruit preservation. *Int. J. Biol. Macromol.* **2021**, *191*, 706–713.

[37] Pitpisutkul, V.; Prachayawarakorn, J. Porous antimicrobial crosslinked film of hydroxypropyl methylcellulose/carboxymethyl starch incorporating Gallic acid for wound dressing application. *Int. J. Biol. Macromol.* **2024**, *256*, 128231.

[38] Cheng, Y.; Zhou, Y.; Wang, R. R.; Chan, K. H.; Liu, Y.; Ding, T. P.; Wang, X. Q.; Li, T. T.; Ho, G. W. An elastic and damage-tolerant dry epidermal patch with robust skin adhesion for bioelectronic interfacing. *ACS Nano* **2022**, *16*, 18608–18620.

[39] Hou, M. J.; Yu, M. L.; Liu, W. L.; Zhang, H. Y.; Wang, Z. S.; Du, J. J.; Xu, L. J.; Li, N.; Xu, J. X. Mxene hybrid conductive hydrogels with mechanical flexibility, frost-resistance, photothermoelectric conversion characteristics and their multiple applications in sensing. *Chem. Eng. J.* **2024**, *483*, 149299.

[40] Zheng, Z. J.; Yang, L.; Yang, Y. P.; Li, L. J.; Lin, B. F.; Fu, L. H.; Xu, C. H. Flexible, sensitive and rapid humidity-responsive sensor based on rubber/aldehyde-modified sodium carboxymethyl starch for human respiratory detection. *Carbohydr. Polym.* **2023**, *306*, 120625.

[41] Pei, X. Y.; Sun, M. M.; Wang, J. J.; Bai, J.; Bo, X. J.; Zhou, M. A bifunctional fully integrated wearable tracker for epidermal sweat and wound exudate multiple biomarkers monitoring. *Small* **2022**, *18*, 2205061.

[42] Chen, Z. H.; Bi, H. J.; Wang, J. W.; Ma, R. Y.; Wang, Y.; Dong, B. Q.; Lu, C. N.; Wang, J. L.; Li, Y.; Zheng, J. et al. Carboxymethyl chitosan/oxidized carboxymethyl starch Schiff base hydrogels containing fasudil for islet encapsulation and transplantation. *Carbohydr. Polym.* **2025**, *368*, 124069.

[43] Tian, X. H.; Wen, Y. T.; Zhang, Z. X.; Zhu, J. L.; Song, X.; Phan, T. T.; Li, J. Recent advances in smart hydrogels derived from polysaccharides and their applications for wound dressing and healing. *Biomaterials* **2025**, *318*, 123134.

[44] Wang, C. R.; Fan, K. X.; Shirzaei Sani, E.; Lasalde-Ramírez, J. A.; Heng, W. Z.; Min, J. H.; Solomon, S. A.; Wang, M. Q.; Li, J. H.; Han, H. et al. A microfluidic wearable device for wound exudate management and analysis in human chronic wounds. *Sci. Transl. Med.* **2025**, *17*, eadt0882.

[45] Song, S. S.; Xu, G. P.; Wang, B.; Liu, D. Q.; Ren, Z. C.; Wang, C. Y.; Zhao, J. P.; Zhang, L. P.; Li, Y. A multifunctional flexible electronic skin for dynamic thermal radiation regulation and electromagnetic interference shielding. *ACS Appl. Mater. Interfaces* **2022**, *14*, 52379–52389.

[46] Wang, C. B.; Liang, Y. Q.; Huang, Y.; Li, M.; Guo, B. L. Porous photothermal antibacterial antioxidant dual-crosslinked cryogel based on hyaluronic acid/ polydopamine for non-compressible hemostasis and infectious wound repair. *J. Mater. Sci. Technol.* **2022**, *121*, 207–219.

[47] Karimi, T.; Mottaghitalab, F.; Keshvari, H.; Farokhi, M. Carboxymethyl chitosan/sodium carboxymethyl cellulose/agarose hydrogel dressings containing silk fibroin/polydopamine nanoparticles for antibiotic delivery. *J. Drug Deliv. Sci. Technol.* **2023**, *80*, 104134.

[48] Wu, X. X.; Li, W. J.; Herlah, L.; Koch, M.; Wang, H.; Schirhagl, R.; Włodarczyk-Biegun, M. K. Melt electrowritten poly-lactic acid /nanodiamond scaffolds towards wound-healing patches. *Mater. Today Bio.* **2024**, *26*, 101112.

[49] Nguyen, N.; Lin, Z. H.; Barman, S. R.; Korupalli, C.; Cheng, J. Y.; Song, N. X.; Chang, Y.; Mi, F. L.; Song, H. L.; Sung, H. W. et al. Engineering an integrated electroactive dressing to accelerate wound healing and monitor noninvasively progress of healing. *Nano Energy* **2022**, *99*, 107393.

[50] Cai, J. H.; Liu, S. H.; Zhong, Q. L.; Shang, Y. F.; Chen, Z. R.; Yao, Y.; Zhou, B.; Yin, F. Y.; Zhao, J. M.; Zheng, L. Multifunctional PDA/ZIF8 based hydrogel dressing modulates the microenvironment to accelerate chronic wound healing by ROS scavenging and macrophage polarization. *Chem. Eng. J.* **2024**, *487*, 150632.

[51] Panwar, V.; Sharma, A.; Murugesan, P.; Salaria, N.; Ghosh, D. Free-flowing, self-crosslinking, carboxymethyl starch and carboxymethyl cellulose microgels, as smart hydrogel dressings for wound repair. *Int. J. Biol. Macromol.* **2023**, *246*, 125735.

[52] Zeng, Q. K.; Peng, Q. W.; Wang, F. B.; Shi, G. Y.; Haick, H.; Zhang, M. Tailoring food biopolymers into biogels for regenerative wound healing and versatile skin bioelectronics. *Nano Micro Lett.* **2023**, *15*, 153.

[53] Liu, X. S.; Chen, F.; Zhang, Y. F.; Zheng, Z. X.; Huang, R.; Tian, J. H.; Li, H.; Zhou, C. R.; Zhang, S. Y.; Xu, H. H. et al. Self-healing sodium alginate-PEDOT:PSS conductive hydrogel for accelerated burn wound healing and real-time monitoring. *Chem. Eng. J.* **2025**, *522*, 167411.

[54] Xin, J. W.; Gao, L. H.; Zhang, W. J.; Song, X. Y.; Yang, Y. M.; Li, W. R.; Zhou, X. H.; Zhang, H. Z.; Wang, Z.; Wang, Z. X. et al. A thermogalvanic cell dressing for smart wound monitoring and accelerated healing. *Nat. Biomed. Eng.* **2026**, *10*, 80–93.

[55] Huang, R. K.; Zhang, X. X.; Li, W. Z.; Shang, L. R.; Wang, H.; Zhao, Y. J. Suction cups-inspired adhesive patch with tailorable patterns for versatile wound healing. *Adv. Sci.* **2021**, *8*, 2100201.

[56] Dong, T.; Hu, J.; Dong, Y.; Yu, Z. Y.; Liu, C.; Wang, G. F.; Chen, S. Advanced biomedical and electronic dual-function skin patch created through microfluidic-regulated 3D bioprinting. *Bioact. Mater.* **2024**, *40*, 261–274.

[57] Choi, G.; Kim, J.; Kim, H.; Bae, H.; Kim, B. J.; Lee, H. J.; Jang, H.; Seong, M.; Tawfik, S. M.; Kim, J. J. et al. Motion-adaptive tessellated skin patches with switchable adhesion for wearable electronics. *Adv. Mater.* **2025**, *37*, 2412271.

[58] Pu, J. Y.; Zhang, Y. T.; Ning, H. M.; Tian, Y. H.; Xiang, C. X.; Zhao, H.; Liu, Y. F.; Lee, A.; Gong, X. L.; Hu, N. et al. Dual-dielectric-layer-based iontronic pressure sensor coupling ultrahigh sensitivity and wide-range detection for temperature/pressure dual-mode sensing. *Adv. Mater.* **2025**, *37*, e03926.

[59] Wang, W. Y.; Yao, D. J.; Wang, H.; Ding, Q. L.; Luo, Y. B.; Ding, H. J.; Yu, J. H.; Zhang, H.; Tao, K.; Zhang, S. et al. A breathable, stretchable, and self-calibrated multimodal electronic skin based on hydrogel microstructures for wireless wearables. *Adv. Funct. Mater.* **2024**, *34*, 2316339.

[60] Wu, L. D.; Qin, H. Y.; Li, Y. X.; Zhao, J. X.; Sun, M. M.; Li, P. Y.; Zhai, X. J.; Wen, Y. H.; Wang, X. H.; Lin, C. T. et al. Thermal-sensitive artificial ionic skin with environmental stability and self-healing property. *ACS Appl. Mater. Interfaces* **2025**, *17*, 9115–9124.

[61] Ai, C.; Song, Y. J.; Liu, C. Y.; An, H.; Yu, P.; Wang, H. C.; Xiang, Y. M.; Yang, J.; Zhang, X. R.; Yeung, K. W. K. et al. A contractile-programmable sensor patch with antibacterial and immunomodulatory properties for infected wound management. *Chem. Eng. J.* **2025**, *520*, 165962.

[62] Xu, G.; Lu, Y. L.; Cheng, C.; Li, X.; Xu, J.; Liu, Z. Y.; Liu, J. L.; Liu, G.; Shi, Z. H.; Chen, Z. T. et al. Battery-free and wireless smart wound dressing for wound infection monitoring and electrically controlled on-demand drug delivery. *Adv. Funct. Mater.* **2021**, *31*, 2100852.

[63] W.; Trotsyuk, A. A.; Niu, S. M.; Henn, D.; Chen, K.; Shih, C. C.; Larson, M. R.; Mermin-Bunnell, A. M.; Mittal, S.; Lai, J. C. et al. Wireless, closed-loop, smart bandage with integrated sensors and stimulators for advanced wound care and accelerated healing. *Nat. Biotechnol.* **2023**, *41*, 652–662.

[64] Jin, T. S.; Wang, H. Y.; Ullah, I.; Xie, W. J.; Lin, T. A.; Tan, Q. L.; Pan, X. Y.; Yuan, Y. Y. A wireless operated flexible bioelectronic microneedle patch for actively controlled transdermal drug delivery. *Adv. Mater.* **2025**, *37*, 2417136.

[65] Zhou, Q.; Chen, W. J.; Wang, H.; Wu, C. C.; Zhu, Q. Q.; Luo, L.; Zheng, X.; Yu, C. L.; Guo, A. J.; Wang, J. J. et al. Porous sodium carboxymethyl starch microspheres for hemostasis and skin wound healing. *ACS Appl. Bio Mater.* **2025**, *8*, 3076–3085.

[66] Yang, J. Y.; Chen, Y.; Zhao, L.; Feng, Z. P.; Peng, K. L.; Wei, A. L.; Wang, Y. L.; Tong, Z. R.; Cheng, B. Preparation of a chitosan/carboxymethyl chitosan/AgNPs polyelectrolyte composite physical hydrogel with self-healing ability, antibacterial properties, and good biosafety simultaneously, and its application as a wound dressing. *Compos. B: Eng.* **2020**, *197*, 108139.

[67] Qiao, C. Y.; Fu, L. H.; Lv, X. H.; Wang, S. X.; Ling, Y. F.; Xu, C. H.; Lin, B. F.; Wei, Y. Hybrid cross-linked sodium carboxymethyl starch/polyacrylamide flexible sensing hydrogels with adhesion, antimicrobial properties and multiple responses. *Int. J. Biol. Macromol.* **2023**, *249*, 126020.

[68] Jiang, Y. N.; Zhang, X.; Zhang, W.; Wang, M. H.; Yan, L. W.; Wang, K. F.; Han, L.; Lu, X. Infant skin friendly adhesive hydrogel patch activated at body temperature for bioelectronics securing and diabetic wound healing. *ACS Nano* **2022**, *16*, 8662–8676.

[69] Li, W. Z.; Yu, Y. R.; Huang, R. K.; Wang, X. C.; Lai, P. X.; Chen, K.; Shang, L. R.; Zhao, Y. J. Multi-bioinspired functional conductive hydrogel patches for wound healing management. *Adv. Sci.* **2023**, *10*, 2301479.

[70] Wu, J. Z.; Liu, Y. J.; Hua, S. M.; Meng, F. J.; Ma, Q. L.; Song, S. L.; Che, Y. J. Dynamic cross-linking network construction of carboxymethyl starch enabling temperature and strain bimodal film sensors. *ACS Appl. Mater. Interfaces* **2023**, *15*, 17293–17300.

[71] Li, M.; Liang, Y. P.; Liang, Y. Q.; Pan, G. Y.; Guo, B. L. Injectable stretchable self-healing dual dynamic network hydrogel as adhesive anti-oxidant wound dressing for photothermal clearance of bacteria and promoting wound healing of MRSA infected motion wounds. *Chem. Eng. J.* **2022**, *427*, 132039.